Bioactive Materials 39 (2024) 25–40

Contents lists available at ScienceDirect

Bioactive Materials

journal homepage: www.keaipublishing.com/en/journals/bioactive-materials

A tantalum-containing zirconium-based metallic glass with superior endosseous implant relevant properties

Yunshu Wu [a,b,c,d,1], Feifei Wang [a,b,c,1], Yao Huang [e], Fu Zheng [b,c,f], Yuhao Zeng [a,b,c], Zhen Lu [e], Songlin Wang [d,g,**], Baoan Sun [e,***], Yuchun Sun [a,b,c,*,2]

[a] Center of Digital Dentistry, Peking University School and Hospital of Stomatology, Beijing, 100081, China
[b] National Clinical Research Center for Oral Diseases & National Engineering Research Center of Oral Biomaterials and Digital Medical Devices, Beijing, 100081, China
[c] Beijing Key Laboratory of Digital Stomatology, Beijing, 100081, China
[d] Beijing Laboratory of Oral Health, Capital Medical University, Beijing, 100069, China
[e] Institute of Physics, Chinese Academy of Sciences, Beijing, 100190, China
[f] Department of Orthodontics, Peking University School and Hospital of Stomatology, Beijing, 100081, China
[g] Laboratory of Homeostatic Medicine, School of Medicine, Southern University of Science and Technology, Shenzhen, 518055, China

ARTICLE INFO

Keywords:
Tantalum
Zirconium-based metallic glass
Surface chemistry
Atomic structure
Endosseous implant

ABSTRACT

Zirconium-based metallic glasses (Zr-MGs) are demonstrated to exhibit high mechanical strength, low elastic modulus and excellent biocompatibility, making them promising materials for endosseous implants. Meanwhile, tantalum (Ta) is also well known for its ideal corrosion resistance and biological effects. However, the metal has an elastic modulus as high as 186 GPa which is not comparable to the natural bone (10–30 GPa), and it also has a relative high cost. Here, to fully exploit the advantages of Ta as endosseous implants, a small amount of Ta (as low as 3 at. %) was successfully added into a Zr-MG to generate an advanced functional endosseous implant, $Zr_{58}Cu_{25}Al_{14}Ta_3$ MG, with superior comprehensive properties. Upon carefully dissecting the atomic structure and surface chemistry, the results show that amorphization of Ta enables the uniform distribution in material surface, leading to a significantly improved chemical stability and extensive material-cell contact regulation. Systematical analyses on the immunological, angiogenesis and osteogenesis capability of the material are carried out utilizing the next-generation sequencing, revealing that $Zr_{58}Cu_{25}Al_{14}Ta_3$ MG can regulate angiogenesis through VEGF signaling pathway and osteogenesis via BMP signaling pathway. Animal experiment further confirms a sound osseointegration of $Zr_{58}Cu_{25}Al_{14}Ta_3$ MG in achieving better bone-implant-contact and inducing faster peri-implant bone formation.

1. Introduction

Endosseous implants, such as artificial joints, fracture fixation devices and dental implants, serve to replace and recover the impaired functions and aesthetics of hard tissues. Mechanical behaviors, corrosion resistance, chemical stability and biocompatibility are important relevant properties that influence the long-term functioning of endosseous implants. Metallic biomaterials, including titanium and its alloys, Co–Cr alloys and 316L stainless steel, are widely applied in endosseous implants. However, mismatching elastic modulus, lack of bioactivity, toxic effects and poor tribology were a few aspects that still need to be improved for better material performances [1–3]. Recently, nanomaterial coatings have been widely introduced to metallic implants to improve their biocompatibility, bioactivity and corrosion resistance [4]. Such as the porous TiO_2/ZrO_2 nanocomposite coatings on 316L stainless steel induced favorable surface cellular attachment and thus enhanced

Peer review under responsibility of KeAi Communications Co., Ltd.
* Corresponding author. Center of Digital Dentistry, Peking University School and Hospital of Stomatology, Beijing, 100081, China.
** Corresponding author. Beijing Laboratory of Oral Health, Capital Medical University, Beijing, 100069, China.
*** Corresponding author. Institute of Physics, Chinese Academy of Sciences, Beijing, 100190, China
E-mail addresses: sophiawu0624@163.com (Y. Wu), 2311110616@stu.pku.edu.cn (F. Wang), huangyao@iphy.ac.cn (Y. Huang), zhengfu@pku.edu.cn (F. Zheng), zeng-yuhao@hotmail.com (Y. Zeng), ZhenLu@iphy.ac.cn (Z. Lu), slwang@ccmu.edu.cn (S. Wang), sunba@iphy.ac.cn (B. Sun), kqsyc@bjmu.edu.cn (Y. Sun).
[1] These authors contributed equally to this work.
[2] Lead contact.

https://doi.org/10.1016/j.bioactmat.2024.04.014
Received 21 January 2024; Received in revised form 28 March 2024; Accepted 14 April 2024

cell proliferation [5]. Yet, more efforts are required to refine the existing or explore more nanomaterials that can balance bioactivity, wear resistance and mechanical strength [4].

Tantalum (Ta) was well acknowledged to have excellent osteoinduction effect [6–8]. It exhibited good corrosion resistance by forming stable Ta_2O_5 passive layers [6–8]. The high material surface energy of Ta could increase surface wettability, favorable for cell adhesion and growth [8]. However, the high elastic modulus (186 GPa) was undesirable for endosseous implants, while the high density, price and melting point made Ta difficult and expensive to process [4,7,9,10]. With the advance of additive manufacturing, porous tantalum has become a good solution. Researches showed that porous tantalum elevated osteogenesis and achieved faster osseointegration, making it a promising endosseous implant [7,10]. Nevertheless, due to the inherent rationale of porous structure, the elastic modulus and mechanical strength is somehow mutually exclusive, meaning a decrease in elastic modulus is usually accompanied by a decrease in mechanical strength.

The disordered atomic structure of metallic glasses (MGs) endowed them with high mechanical strength and low elastic modulus, which were ideal properties for load-bearing implants that required better bone-match modulus to reduce the stress shielding effect [11,12]. The absence of grain- and phase-boundaries rendered MGs good corrosion and wear resistance, beneficial for long-term safety service in clinical use. Among them, zirconium-based MGs (Zr-MGs) were demonstrated to possess excellent biocompatibility both *in vitro* and *in vivo* [1]. Zr–Cu–Al and their derivatives were well-established for their good glass forming ability, which was a prerequisite for material fabrication with desirable sizes [11].

To combine and maximize the advantageous properties of both Ta and Zr-MGs, we intended to create a new Ta-containing Zr-MGs for endosseous implants. A previous study observed that the solubility limit of Ta in the amorphous phases was approximately 4 at.% in a Zr–Cu–Al–Ni system, yielding a $Zr_{60.2}Ni_{8.6}Cu_{17.2}Al_{10}Ta_4$ MG in 3 mm diameter rod [13]. In the meantime, $Zr_{55}Al_{10}Ni_5Cu_{26}Ta_4$ MG was only reported in 3.5 mm diameter size [14]. Despite the good glass forming ability of Ni in MGs, it showed several clinical allergy issues [15]. To date, 5 at.% of Ta in the Ni-free Zr–Cu–Al system, $Zr_{53}Cu_{33}Al_9Ta_5$, was the maximum content reported to achieve fully amorphous state in a thin film coating of 200 nm, which was insufficient to meet the size demand of endosseous implants [16–18]. Taken these into considerations, we successfully substituted Zr with 3 at.% Ta, creating a new amorphous $Zr_{58}Cu_{25}Al_{14}Ta_3$ (Ta3-A) alloy. Considering the typical disordered atomic structure and uniform surface elemental distribution pattern of MGs, we planned to investigate the influence of Ta addition on endosseous implant relevant properties from the two aspects of atomic structure and surface chemistry. Therefore, we chose crystalline $Zr_{58}Cu_{25}Al_{14}Ta_3$ (Ta3–C) as a microstructural control, $Zr_{61}Cu_{25}Al_{14}$ (Ta0) as a Ta-absent MG control and commercial pure titanium (cpTi) as a state-of-the-art control.

Implant placement could trigger complex regulations involving immune related macrophage responses, angiogenesis of endothelial cells, as well as the most important osteogenesis of bone marrow mesenchymal stem cells (BMSCs) [19]. In this study, we also provided a transcriptomic profiling of material's influence on the three cellular responses that were highly essential for sound osseointegration of endosseous implants.

2. Materials and methods

2.1. Sample preparation

Master alloy ingots of Ta0 and Ta3-A were prepared by arc-melting a mixture of pure elements in an argon atmosphere and subsequent suction casting in copper molds. Cylindrical rods with 3 mm or 5 mm diameter were obtained. 5 mm diameter rods with 1 mm thickness samples were polished to #2000 SiC surface finish, and cleaned successively by acetone and alcohol for cellular studies. 3 mm diameter rods were machined to fabricate implants with 1.5 mm diameter, 12 mm in length, 0.6 mm pitch and 0.4 mm thread depth.

Ta3-A was annealed in vacuum at 600 °C using a box-type resistance-heated furnace (FNS Electric Furnace co., Ltd, Beijing, China) to obtain Ta3–C. Grade 4 commercial pure titanium (purity 99.995 wt%) was used as a reference alloy throughout the whole experiment.

2.2. Material characterization

2.2.1. Structural, thermal and morphological analysis

The microstructure of as-cast and annealed samples was assessed by X-ray diffraction (XRD) (Bruker D8A A25, Germany) with Cu K_α radiation at 40 kV and a 2θ range of 20°–80° for MGs, 20°–100° for crystalline. Peak annotations were analyzed with Jade 6.5 software.

The thermal stability was analyzed with a differential scanning calorimeter (DSC) (NETZSCH, Germany) at a heating rate of 20 K/min to 1200 K, under a continuous argon flow.

The morphological analysis for material microstructure and chemical distribution was carried out with an aberration-corrected transmission electron microscope (TEM, JEOL NEOARM200, Japan) using high angle angular dark field detector under scanning mode (HADDF-STEM). The cellular morphology on material surface was observed with scanning electron microscopy (SEM) (Hitachi S-4800, Japan) at 5 kV acceleration voltage.

2.2.2. Surface characterization

Chemical compositions of material surfaces were analyzed by X-ray photoelectron spectroscopy (XPS) (Thermo Fisher Scientific ESCALAB 250X, USA). Monochromated Al K_α X-ray source of 1486.6 eV was used. XPS etching was performed with in situ XPS ion beam sputtering with argon (Thermo Fisher Scientific Nexsa G2, USA). The binding energy (BE) of the XPS was calibrated with respect to the pure bulk Au $4f_{7/2}$ (BE = 84.0 eV) and Cu $2p_{3/2}$ (BE = 932.7 eV) lines. The BE was referenced to the Fermi level (E_f) calibrated by using pure bulk Ni as $E_f = 0$ eV. The narrow spectra were further deconvoluted with XPSpeak 41 software.

The contact angles of materials investigated were measured by a drop-shape analysis system (JY-82B Kruss DSA, Germany) at room temperature with 2 μl of simulated body fluid (SBF).

2.2.3. Mechanical properties

Material density ρ was measured by micromeritics (AccuPyc II 1345, USA).

Compression strength tests were measured at room temperature on rod samples with 2 mm in diameter and 4 mm in length using a universal testing device (Instron, USA) at a strain rate of 5×10^{-4} s^{-1}.

The ultrasonic measurement was carried out using a CTS-8077PR Pulse Generator and Receiver. Longitudinal (Vp) and transverse (Vs) velocity were detected (Fig. S2C), and then used to calculate the Poisson's ratio υ based on the previous report [20]:

$$\varepsilon = \frac{Vp}{Vs}$$

$$\upsilon = \frac{0.5\varepsilon^2 - 1}{\varepsilon^2 - 1}$$

The young's modulus E could further be calculated based on [21]:

$$Vp = \sqrt{\frac{E}{\rho}} \bullet \sqrt{\frac{1-\upsilon}{1-\upsilon-2\bullet\upsilon^2}}$$

$$Vs = \sqrt{\frac{E}{\rho}} \bullet \sqrt{\frac{1}{2+2\bullet\upsilon}}$$

The hardness and reduced elastic modulus were measured by nanoidentation (Bruker Hysitron TI 980 Tribolndenter, Germany). The elastic recovery curves were acquired at a loading of 10 mN. Ten indents

were made to improve the statistics.

2.2.4. Electrochemical behaviors

Tested samples were first embedded in an epoxy resin exposing an 1 cm^2 testing area, which were subsequently polished to #2000 SiC surface finish and cleaned with ethanol. Potentiodynamic polarization curves was tested in SBF using an electrochemical workstation (Princeton Versa STAT 3F) at 37 °C. The electrochemical tests were performed in a three-electrode system with a platinum electrode as the counter electrode and a saturated calomel electrode (SCE) as the reference electrode. Open circuit potential were tested for 30 min to stabilize the potential. The polarization curves were scanned from −750 mV to +250 mV relative to the open circuit potential at a rate of 1 mV/s.

2.2.5. Inductively coupled plasma-mass spectrum

Sample disks of investigated materials (5 mm in diameter and 1 mm in thickness) were fully immersed in 200 μl α-MEM media (Hyclone, USA) at 37 °C for 1, 3, 5, 7 and 14 days, *respectively*. For cell pellet sample, the sample was digested with 0.1 mL of nitric acid at 65 °C for 1 h, and then diluted with 0.1 mL of water. Ion concentration of Zr, Cu, Al, Ta and Ti were determined by inductively coupled plasma-mass spectrum (ICP-MS, PerkinElmer, USA).

2.3. In vitro measurements

2.3.1. Isolation of BMSCs and cell culture

The study protocol was approved by the Medical Ethical Commission of the Peking University School and Hospital of Stomatology (PKUSSIRB-202169161). Patients undergoing orthognathic surgery were selected after signing an informed consent. The resected bone blocks were cut into pieces and then subjected to 10 % collagenase type II (Worthington, USA) for 1 h before culturing in the Petri dish. BMSCs were cultured in α-MEM media (Hyclone, USA) supplemented with 10 % fetal bovine serum (FBS) (Gibco, USA), 100 units/mL penicillin (Gibco) and 100 μg/mL streptomycin (Gibco), at 37 °C with an atmosphere of 5 % CO_2 and 95 % humidity.

For osteogenic induction, BMSCs were treated with osteogenic medium containing 50 μg/mL ascorbic acid, 5 mM β-glycerophosphate, and 100 nM dexamethasone (all from Sigma).

2.3.2. Cell adhesion assay

BMSCs were seeded on prepared material samples in 96-well plates for 1, 4 and 24 h. After washing twice with PBS (Gibco) to remove unadherent cells, adherent cells were fixed with 4 % PFA (Solarbio, China) for 15 min at room temperature and then stained with DAPI (Sigma). Immunofluorescent images were observed and captured using a laser scanning confocal microscope (Nikon Eclipse T*i*2, Japan). The cell numbers were counted in 5 random fields and analyzed using Image J software (National Institutes of Health, Bethesda, MD, USA).

2.3.3. Cell viability and proliferation

Live/dead Staining: After incubating with material samples for 24 h, 3 and 7 days, BMSCs were washed with PBS twice, and then stained with calcein-AM and PI (Solarbio) for 30 min at room temperature according to the manufacturer's protocol.

The BMSCs cell viability test for 1, 3, 5 and 7 days was performed using cell titer-glo (Promega, USA) according to manufacturer's protocol and luminescence was measured using a chemiluminescence microplate reader (SpectraMax i3x, USA).

The cell viability staining on day 5 of co-culturing was determined using Fortessa flow cytometry (BD FACS, USA). BMSCs were digested with 0.25 % trypsin for 5 min at 37 °C, washed with PBS and then stained with fixable viability stain 520 (BD Bioscience) for 30 min according to manufacturer's protocol. Data were analyzed with FlowJo v10.8.1.

For cell proliferation assay, HUVECs (purchased from iCell Bioscience, China) were plated on prepared material samples in 96-well plates for 1, 3, 5 and 7 days in ECM media (Sciencell, USA). HUVECs were incubated with cell counting kit-8 reagent (Dojindo Laboratories, Japan) for 3 h and the OD value was determined using a spectrophotometer (BioTek, USA) at A450 nm.

2.3.4. Phalloidin staining

After incubating with material samples for 24 h, BMSCs were washed with PBS twice, fixed with 4 % PFA, incubated with 0.1%Triton-x100 (Sigma) in 5 % bovine serum albumin (Solarbio) for 10 min at room temperature. TRITC Phalloidin (Yeasen, China) staining was used to mark f-actin and DAPI (Sigma) was used for nuclear staining.

2.3.5. Isolation of bone marrow derived macrophages and cell culture

The study protocol was approved by the Ethics Committee for Animal Experiments at Peking University Health Science Center (PUIRB-LA2023513). Primary macrophages were flushed out from the femoral bone marrow of 6–8 weeks old C57BL/6J mice. After lysing red blood cells (Beyotime, China), cells were cultured in DMEM (Hyclone) supplemented with 10 % FBS, 100 units/mL penicillin (Gibco), 100 μg/mL streptomycin (Gibco), and 30 ng/mL of macrophage colony-stimulating factor (M-CSF) (PeproTech, USA) at 37 °C with an atmosphere of 5 % CO_2 and 95 % humidity to obtain naive macrophages. Passage 3 macrophages were seeded on prepared material samples for 48 h.

2.3.6. Scratch assay

Material extracts were prepared according to ISO 10993-12-2021. In brief, disinfected materials were fully immersed in ECM media and sealed in centrifuged tubes (Corning, USA) for 72 h at 37 °C. The ion release levels of different materials were evaluated by ICP-MS.

HUVECs were seeded in 12-well plate in normal ECM media overnight, then changed into material extracts. A linear wound was performed with a sterile 1 mL pipette tip. The migration of HUVECs was recorded by an optical microscopy (Olympus, Japan).

2.3.7. Tube formation assay

HUVECs were pretreated with material extracts for 24 h and then seeded on growth factor-depleted Matrigel (BD Bioscience) in 48-well plates. The tube formation of HUVECs was recorded by an optical microscopy (Olympus, Japan) and quantitative analyses were performed using Image J software.

2.3.8. Immunofluorescent staining

HUVECs were cultured with material samples for 3 days and washed twice with PBS. HUVECs were fixed with methanol (Merck, USA) in −20 °C for 15 min and then permeated in 0.1%Triton-x100 in 5 % goat serum (Solarbio) for 5 min at room temperature. Primary antibody of VEGFA rabbit pAb (A12303, Abclonal, China) was diluted at 1:100 in 5 % goat serum and incubated on HUVECs at 4 °C overnight. Then HUVECs were stained with a secondary antibody of FITC Goat anti-Rabbit IgG (H + L) (AS011, Abclonal, China) at 1:100 in 5 % goat serum for 1 h at room temperature. DAPI was stained for nuclear imaging. Immunofluorescent images were observed and captured using a laser scanning confocal microscope (Nikon Eclipse T*i*2, Japan). The mean intensity was counted in 5 random fields and analyzed using Image J software.

2.3.9. ALP, ARS staining and quantification

For ALP staining, BMSCs were co-cultured with material samples and fixed after 7 days induction of osteogenic differentiation with 4 % PFA for 15 min and incubated with BCIP/NBT solution according to manufacturer's protocol (Beyotime). For quantitative ALP activity, BMSCs were lysed with RIPA buffer (Beyotime), the supernatant was then detected using a commercial kit according to the manufacturer's protocol (Beyotime). The optical density was determined by a spectrophotometer (BioTek, USA) at A450 nm.

For alizarin red S (ARS) staining, BMSCs were co-cultured with material samples and fixed after 14 days induction of osteogenic differentiation with 4 % PFA for 15 min and stained with Alizarin red S solution (Cyagen, China) for 15 min. Mineralized matrix stained with alizarin red S was destained with 10 % cetylpyridinium chloride (Sigma) in 10 mM sodium phosphate (pH 7.0) (Sigma), and the calcium concentration was determined by a spectrophotometer (BioTek, USA) at A562 nm.

2.3.10. Quantitative real-time PCR

Total RNA of cultured cells was extracted using Trizol (Invitrogen) according to manufacturer's instruction. cDNA was prepared using PrimeScript RT reagent Kit with gDNA Eraser (Takara). The RNA concentration was measured with a NanoDrop 2000 (Thermo Fisher Scientific). qRT-PCR was performed using NovoStartSYBR qPCR SuperMix plus (Novoprotein, China) in CFX96 Real-Time System (Bio-Rad). Relative gene expression was normalized by GAPDH using a $2-\Delta\Delta Ct$ method. The primers are listed in Supplementary Table 1.

2.3.11. Western blot

Cells were lysed in RIPA buffer (Beyotime) on ice and the supernatants were collected. Protein concentrations were measured using BCA assay (Beyotime) according to manufacturer's instruction. The proteins were heated at 95 °C for 5 min in sample buffer containing 2 % SDS and 1 % 2-mercaptoethanol, separated on 10 % SDS–polyacrylamide gels, and transferred to PVDF membranes by Trans-Blot Turbo (Bio-Rad). The membranes were blotted with 5 % non-fat dry milk (Sigma) for 1 h and then incubated overnight with CD80 Rabbit mAb (1:1000, Abclonal, Cat No: A23688), Mannose Receptor/CD206 Rabbit mAb (1:1000, Abclonal, Cat No: A21014), iNOS Polyclonal antibody (1:1000, Proteintech, Cat No: 22226-1-AP), BMP4 Polyclonal antibody (1:1000, Proteintech, Cat No: 12492-1-AP), SMAD9 Polyclonal antibody (1:1000, Proteintech, Cat No: 16397-1-AP), *p*-SMAD1/5/8 Rabbit mAb (1:1000, Cell Signaling, Cat No: 13820T), Alkaline Phosphate (ALPL) Rabbit mAb (1:1000, Abclonal, Cat No: A0514), Rabbit Anti-beta-Actin/HRP antibody (1:1000, Bioss, Cat No: bsm-52846R), followed by incubation with a goat anti-rabbit IgG secondary antibody HRP conjugated (1:1000, Beyotime, Cat No: A0208). The antibody-antigen complexes were visualized with ECL (Bio-rad), and exposed with ChemiDoc MP imaging system (Bio-rad).

2.3.12. RNA-sequencing and gene set enrichment analysis

Total RNAs were extracted by Trizol reagent and purified using poly-T oligo-attached magnetic beads. Sequencing libraries were generated using NEBNext® Ultra™ RNA Library Prep Kit for Illumina® (NEB, USA) following manufacturer's recommendations, and were then subjected to Illumina HiSeq 2500. We used FastQC (v0.11.5) and FASTX toolkit (0.0.13) to control the quality of RNA-seq data and mapped them to Homo Sapiens or Mus musculus reference genomes using HISAT2 (v.2.0.5). DESeq2 software (v.1.20.0) was performed to identify differentially expressed genes and transcripts. Genes were considered significantly differentially expressed if showing $|\text{Log}_2 \text{(Fold Change)}| \geq 1.0$ and $padj < 0.05$.

GO and KEGG analysis based on differentially expressed genes were performed with cluster Profiler (3.8.1) and were considered significantly differentially expressed if showing *padj* value < 0.05. GSEA were performed with gsea software (v3.0).

2.4. In vivo measurements

2.4.1. Implantation surgery and tissue collection

The study protocol was approved by the Ethics Committee for Animal Experiments at Peking University Health Science Center (PUIRB-LA2023268). 36 male Sprague-Dawley rats were randomly assigned into the cpTi, Ta0 and Ta3-A groups (n = 6 for each group in each time point). The right leg of each rat was shaved and disinfected after general anesthesia, and a medial parapatellar arthrotomy was performed to expose the right intercondylar fossa. A 15 mm long bone marrow tunnel was drilled through the intercondylar fossa with a 1.5 mm diameter drill, and prepared material implants were inserted into the tunnel (Fig. S9). Wounds were closely sutured using 3–0 absorbable threads. For the 8-week group, a sequence of fluorochrome labels with alizarin complexone (20 mg/kg, Sigma) and calcein green (20 mg/kg, Sigma) was injected at 4 weeks post-surgery and 3 days before sacrifice, *respectively*.

The animals were sacrificed at 4 and 8 weeks after implant surgery. 1.5 mL blood was collected from eye socket vein for biochemical test. Femurs with implants, liver and kidney were harvested and fixed in 4 % PFA for subsequent processes.

2.4.2. High-resolution Micro-CT evaluation

Femurs with implants were scanned using a high-resolution micro-CT (Phoenix v|tome|x m, Baker Hughes, USA) with 200 kV, 50 μA, 10 μm spatial resolution. The region of interest (ROI) was defined as a column at the center of the bone tunnel of 2 mm in diameter and 2 mm in length, 1.5 mm above the growth plate of the condyles, and was analyzed using Skyscan CT-analyzer software (Bruker).

2.4.3. Histological analysis

Femurs with implants were dehydrated by increasing concentrations of ethanol (60 %, 80 %, 90 %, 100 %) and embedded in light-curing epoxy resin. The embedded specimens were cut perpendicular to the long axis of the implant and ground to around 60 μm thickness using a grinding machine (Exakt, Germany). Fluorescent signals of sequential labeling were observed using a fluorescent microscope (Olympus, Japan). Sections were stained with Stevenel's blue and Van Gieson's picrofuchsin stain and then observed under a light microscope (Olympus, Japan).

Histomorphometric measurements of bone area (BA) and bone-implant contact (BIC) were measured with Image J software. BA was defined as the proportion of bone volume to total tissue volume in the 200-μm-wide circular area around the femur implant surface. BIC was defined as the percentage of the implant circumference in which direct bone-to-implant contact was recorded.

2.5. Statistical analysis

Statistical differences were analyzed by one-way ANOVA followed by Tukey's post hoc test for multiple comparisons using SPSS ver24. Asterisks denote statistical significance as follows: $*p < 0.05$, $**p < 0.01$ and $***p < 0.001$.

3. Results and discussion

3.1. Structural properties, thermal parameters and surface chemical compositions

The X-ray diffraction (XRD) pattern of as-cast Ta0 and Ta3-A in 5-mm rods demonstrated the classical single-phase amorphous structure, without any Bragg peaks (Fig. 1A and Fig. S1A). Ta0 showed a single exotherm in its differential scanning calorimetry (DSC) trace while Ta3-A exhibited two exothermic peaks corresponding to two distinct stages of phase separations. It was observed that Ta might promote composition separation and multiple-stage crystallization. 2 at.% and 4 at.% amount of Ta addition induced the appearance of a second exothermic peak, and 6 at.% of Ta had a DSC feature of four exotherms, in contrast to their 0 at.% Ta counterparts [13,14]. The glass transition temperature (T_g) for Ta0 and Ta3-A were 396 °C and 413 °C, *respectively* (Fig. 1B). The onset crystallization temperature (T_x) were 462 °C and 482 °C, *respectively*. The supercooled liquid region (ΔT) between T_x and T_g for both MGs exceeded 50 °C, indicating good glass-forming ability [22]. A crystalline counterpart of Ta3–C was fabricated by annealing samples to

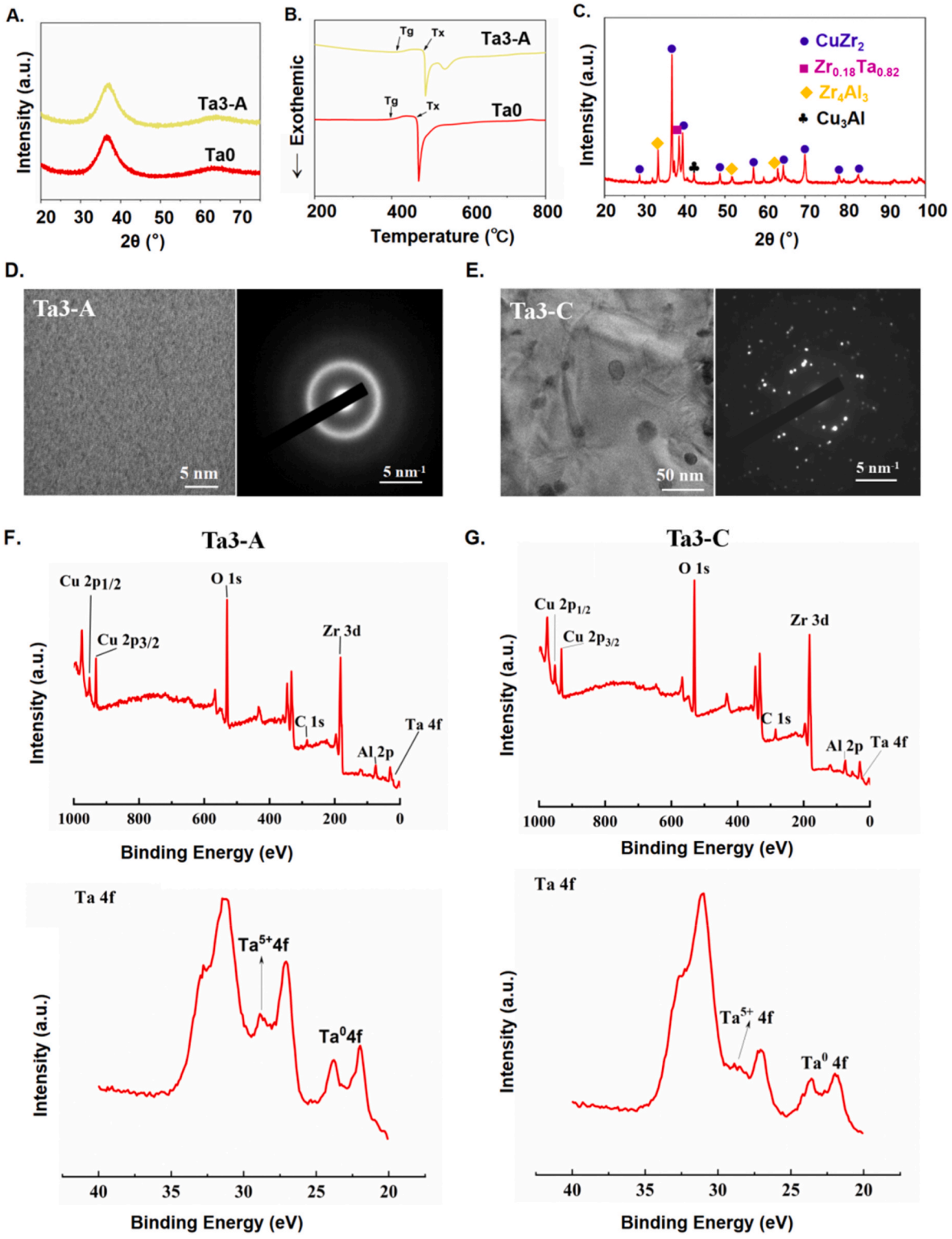

Fig. 1. Structural properties, thermal parameters and surface chemical compositions of Ta0, Ta3-A and Ta3–C. A) Representative XRD pattern of Ta0 and Ta3-A. B) Representative DSC data of Ta0 and Ta3-A, showing their transition temperature (T_g) and crystallization temperature (T_x). C) Representative XRD pattern of Ta3–C, showing major crystal phases of $CuZr_2$, $Zr_{0.18}Ta_{0.82}$, Zr_4Al_3 and Cu_3Al. D) Microstructure and SAED pattern of Ta3-A, showing microstructural homogeneity and the amorphous ring. E) Microstructure and SAED pattern of Ta3–C, showing the presence of nanocrystalline and crystalline spots. F) XPS survey spectrum and narrow scan spectra of Ta for Ta3-A. Ta_2O_5 was detected in the oxide film formed on the surface of Ta3-A. G) XPS survey spectrum and narrow scan spectra of Ta for Ta3–C. Ta_2O_5 was less potentially presented in the oxide film formed on the surface of Ta3–C.

600 °C, so as to set a fully crystalline microstructural control to evaluate the function of Ta in amorphous state. Distinct Bragg peaks of Ta3–C were analyzed by Jade and major crystal phases were defined as $CuZr_2$, $Zr_{0.18}Ta_{0.82}$, Zr_4Al_3 and Cu_3Al (Fig. 1C).

Microstructural homogeneity of Ta0 and Ta3-A was carefully scrutinized by transmission electron microscope (TEM) and two diffuse halos featuring the short-range order of MGs confirmed the amorphous state of the two alloys (Fig. 1D and Fig. S1B). The distinct phase boundaries in TEM and sharp spots on selected area electron diffraction (SAED) pattern verified the presence of nanocrystalline (Fig. 1E).

X-ray photoelectron spectrometer (XPS) identified the presence of Zr, Cu, Al, O in Ta0, Zr, Cu, Al, Ta, O in Ta3-A and Ta3–C (Fig. 1F, G and Figs. S1C–E), confirming our elemental composition. The narrow spectra for each element revealed that the predominant state of Zr element on the surface was Zr^{4+}, identified as $3d_{5/2}$ and $3d_{3/2}$ doublet peaks approximate to 182 eV and 184 eV, *respectively*. Al was also enriched in an oxide form of Al^{3+} 2p, whereas major proportion of Cu existed in the form of metal as detected as Cu^0 $2p_{3/2}$ and $2p_{1/2}$. Similarly, Ta 4f could be deconvoluted as an oxide form of Ta^{5+}, which was most likely to be Ta_2O_5 based on the binding energy around 26.2 eV and an interval of 1.92 eV between doublet peaks, and a metal form of Ta^0 around 21.8 eV [23]. Interestingly, the Ta^{5+} doublet peaks were more obvious and broad in Ta3-A compared to that of the Ta3-C, indicating increased proportion of Ta_2O_5 in Ta3-A surface oxide layer that might promote corrosion resistance [6–8].

3.2. Mechanical properties, corrosion resistance and hydrophilic characterization

Densities were listed in Table 1. It was worth mentioning that the relative change of density from Ta3-A to Ta3–C was 0.58 %. The increase in density upon crystallization was proposed as a result of reduced free volume content in MGs, which was typically about 0.5 % and as large as 1 % occasionally [11].

The compressive strength of Ta0 (1689.41 MPa) and Ta3-A (1753.19 MPa) were 3-fold higher than cpTi (550.33 MPa) (Table 1 and Fig. S2A). Crystallization significantly reduced the compressive strength of Ta3–C, due to the presence of crystal defects such as dislocations and slip planes [24].

The Young's modulus of Ta0 and Ta3-A was 88 GPa and 91 GPa (Table 1), *respectively*, which were lower than the reported 110 GPa for cpTi, in line with published results [1,22,25,26]. Ta3-A reduced about 35 % of Young's modulus compared to its crystalline counterpart, in accord with the review of Bernard et al. [27]. Indeed, the current Young's modulus of Ta3-A was still higher than that of the natural bone (10–30 GPa), but might be relatively more advantageous than cpTi and pure Ta (186 GPa) in reducing the stress shielding effect [28]. Nanoindentation results confirmed that Ta0 and Ta3-A had lower reduced elastic modulus (E_r) and higher hardness (H) than cpTi. The hardness of Ta3-A increased by approximately 33.8 % upon crystallization. Annealed at higher temperature, the metallic glasses were reported to show an obvious increase in hardness under low applied loads, which could be attributed to the formation of hard intermetallic phases during annealing and embedded nanocrystalline in the amorphous matrix [29–31]. The H/E_r ratio is related to wear resistance and H^3/E_r^2 is proportional to the resistance of the material to plastic deformation [30,32]. Two MGs demonstrated an apparent advantage over cpTi in both aspects, as reported [1]. Meanwhile, Ta3–C had slightly better resistance to plastic deformation and lower wear resistance in contrast to the Ta3-A (Table 1). It was found in Zr- and Ti- based MGs that the best wear performance tended to take place in a partially crystallized state, with nanocrystalline dispersing in amorphous matrix [31,33].

Potentiodynamic anodic polarization measurements and Tafel curves were shown in Fig. 2A. The corrosion potential of cpTi was significantly more positive in contrast to Ta3-A, yet it also exhibited the significantly highest passive current density, indicating a faster corrosion rate. Both Ta3-A and Ta3–C showed better corrosion behavior in physiologically relevant environment than Ta0. Pitting corrosion in chloride-containing solution was an inherent defect in Zr-MGs, as Cl ions brokedown the protective passive film and re-exposed MGs to corrosive solutions [11,22,25]. The improved corrosion resistance due to Ta addition in metal alloys could be achieved at a small proportion of 2 wt % and continued to increase with increasing Ta content by forming a higher chemically stable oxide film [8,11,34]. The tested electrochemical parameters of Ta3-A were slightly, yet not statistically, inferior than that of Ta3–C. When polished to a 600-grit SiC finish, $Zr_{52.5}Cu_{17.9}Ni_{14.6}Ti_5Al_{10}$ also exhibited slightly higher i_{corr} and corrosion penetration rates than its annealed crystalline counterpart, which were 1.2 ± 0.6 mA/m^2 and 1.3 ± 0.7 μm/year, *respectively*, for the amorphous material, and 0.5 ± 0.3 mA/m^2 and 0.6 ± 0.3 μm/year, *respectively*, for the crystalline material [35]. Therefore, the authors suggested that the homogeneity of the amorphous structure alone might not be sufficient to impart general or localized corrosion resistance to Zr-MGs [11,35,36].

Ta0 had the significantly highest contact angle of 54.77° ± 0.28°, while the contact angle for cpTi, Ta3-A and Ta3–C was 47.7° ± 0.26°, 49.25° ± 2.28° and 48.25° ± 0.69° (Fig. 2B), *respectively*. Moderately wettable surfaces with a water contact angle of ~40°–~70° were considered to have a balanced preference for both cell and protein adhesion, and was proved to promote endothelial cell adhesion and growth [8]. The surface energy of Ta (54.6 mJ/m^2) was higher than Zr (43.87 mJ/m^2), therefore the substitution of Zr with 3 at.% Ta in Ta3-A contributed to the enhanced wettability [37]. The stronger binding of water molecules on more hydrophilic surface of Ta3-A would in turn interact with the Ta^{5+} and O^{2-} ions in the surface oxide layer to induce more oxide formation, which further helped to elevate corrosion and wear resistance [8].

3.3. Cell adhesion, morphology and viability features

Biosafety is the utmost prerequisite for biomedical materials. BMSCs were seeded on the materials for 1 h, 4 h and 24 h to assess the influence of surface chemistry and atomic structure on cell adhesion (Fig. 3A and Fig. S3A). We observed an inferior initial cell adhesion at 1 h and 4 h on Ta0 surface compared to cpTi and Ta3-A, which could be well explained by its higher contact angle. BMSCs adhered less on Ta3–C at 1 h and 4 h time-point compared to its amorphous form. Crystallization created grain or phase boundaries that had been shown to affect material surface

Table 1
Density, compressive stress, young's modulus and nanoindentation results.

Materials	Density (g/cm^3)	Compressive stress (MPa)	Young's modulus (GPa)	Poisson's ratio (ν)	Reduced Young's modulus (Er) (GPa)	Nano hardness (H) (GPa)	H/Er (μm)	H^3/Er^2 (GPa)
cpTi	4.78 ± 0.02	550.33 ± 37	110	0.35	125.41 ± 1.40	4.89 ± 0.24	0.039	0.007
Ta0	6.69 ± 0.06	1689.41 ± 161.41	88 ± 1.90	0.36	100.71 ± 0.01	5.80 ± 0.01	0.058	0.020
Ta3-A	6.88 ± 0.01	1753.19 ± 45.10	91 ± 0.67	0.36	101.74 ± 3.58	6.09 ± 0.01	0.060	0.022
Ta3–C	6.92 ± 0.02	733.34 ± 147.72	141 ± 1.51	0.30	142.92 ± 0.16	8.15 ± 0.10	0.057	0.026

Data are presented as mean ± SD.

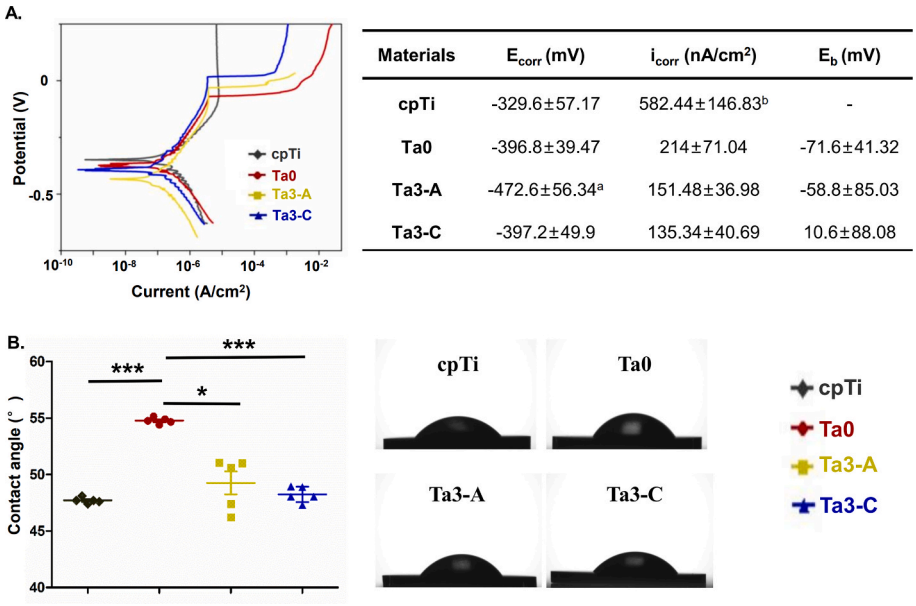

Materials	E_{corr} (mV)	i_{corr} (nA/cm^2)	E_b (mV)
cpTi	-329.6±57.17	582.44±146.83[b]	-
Ta0	-396.8±39.47	214±71.04	-71.6±41.32
Ta3-A	-472.6±56.34[a]	151.48±36.98	-58.8±85.03
Ta3-C	-397.2±49.9	135.34±40.69	10.6±88.08

Fig. 2. Electrochemical results and surface hydrophility. A) Potentiodynamic-polarization curves and corrosion parameters of all samples in simulated body fluid (SBF), indicating a slower corrosion rate of Ta0, Ta3-A and Ta3–C, compared to cpTi. Data are presented as mean ± SD. a: Ta3-A vs cpTi $p < 0.01$; b: cpTi vs the other three $p < 0.001$. B) Contact angles of all samples. Ta0 showed significantly higher contact angle than the other three. Data are presented as mean ± SE. $^*p < 0.05$ and $^{***}p < 0.001$.

charge, protein adsorption and cell adhesion thereafter [38]. There was no significant difference between cpTi and Ta3-A, which was in consistent with a previous report showing that polished Ta and Ti had similar effect on cell attachment number at their inherent material property [39].

Cytoskeleton staining (Fig. 3A and Fig. S3A) and scanning electron microscope (SEM) (Fig. 3B) revealed that BMSCs were more extensively spreading and firmly attached on the Ta3-A compared to Ta3–C. Meanwhile, the cellular morphology was very much alike on different surface chemistry. Crystallized MGs had similar affinity to platelet and fibrin within 48 min of incubation, but compromised bacteria adhesion and cell attachment in 1 h and 48 h, *respectively*, implying a tunable surface biology of MGs to meet functional demands [40–42]. For endosseous implants, well-contacting of BMSCs to material surface is of much importance, so the amorphous state of Ta3-A examined here was more favorable due to its structural homogeneity.

No acute cytotoxicity was observed during the first 24 h, as well as after 3 days, of material-cell co-culturing (Figs. S3B and C). However, BMSCs cultured with Ta–C exhibited obvious cell death and detachment on the 7th day (Fig. S3D). Consistently, instead of continued proliferation, cell viability started to fall in the crystalline group on the 5th day (Fig. 3C). A live/dead flow cytometry was carried out on day 5 to examine cell state. The crystalline group showed a distinct subpopulation in higher fluorescent intensity, indicating necrotic cells (Fig. 3D and Fig. S3E).

In search of potential explanation, materials were immersed in α-MEM media at 37 °C, then subjected to ICP-MS test to measure ion release. Ta0 and Ta3-A exhibited modest increase in metal ion levels within the first week, with Cu being the highest element (Fig. 4A and Fig. S4B), in consistent with another report with the same atomic portion of Cu [2]. Although being higher than cpTi (Fig. S4A), the total ion release of Ta0 and Ta3-A during the observation was much lower than the safe limits to threaten cell viability [43,44]. Researches had shown that Zr-MGs was ready to form and increase a passive oxide film in biological context, accounting for the steady saturation at longer dissolution time [2,45,46]. The presence of Ta_2O_5 improved the stability of this passive film, since Ta3-A almost reached a release plateau between 1 and 2 weeks, while a continued release of Zr, Cu and Al ions proceeded to 2 weeks in Ta0. There was a sharp increase in Zr and Cu ions on day 5 of Ta3–C, which continued to grow rapidly to day 14. The clear boundaries between crystal phases of Ta3–C were responsible for this great distinction in ion release pattern compared to its amorphous counterpart.

Further, we scrutinized the ion intake of BMSCs on day 5 when the significant difference in cell viability and ion release began to show (Fig. 4B and Fig. S4C). The content of Zr ion in Ta3-C was 37.69 ± 8.075 ng/million cells, a sharp contrast to the rest three groups where intracellular Zr level was barely detectable. It was also worth mentioning that the Cu intake of BMSCs in cpTi, Ta0, Ta3-A and Ta3–C was 6.583 ± 0.955 ng/million cells, 7.985 ± 0.665 ng/million cells, 6.446 ± 0.838 ng/million cells, 20.63 ± 5.504 ng/million cells, *respectively*. Tsvetkov et al. tested that intracellular Cu level of approximately 15 ng/million cells could reduce the viability of ABC1 cells to 0.3 after 24 h and 0.15 after 96 h as a result of cuproptosis [47]. BMSCs in Ta3–C also took almost 10-fold higher Al and Ta ions than Ta3-A. In overall, we suggested that changes in atomic structure from Ta3-A to Ta3–C caused a significant increase in total metal ion release, and resulted in an excessive accumulation of intracellular metal contents, leading to compromised BMSCs viability.

STEM-EDS mappings were carried out to evaluate chemical changes on Ta3-A and Ta3–C surface before and after the immersion in α-MEM media at 37 °C for 5 days (Fig. 4C). Elemental distribution in Ta3-A was still uniform and did not change significantly during immersion. Visible crystalline phases were mapped in Ta3–C where Ta was mainly aggregated at a confined region, in an apparent contrast to its evenly distributed amorphous counterpart. Scattered Cu depleted regions appeared in Ta3–C after immersion, implying that any amount of Cu was released from the material surface. The released Cu seemed to coordinate with amino acids in the immersion media that formed a covering layer at the material surface, as evidenced by an overlap with carbon, nitrogen and oxygen (Fig. S4D) [48]. Cu was also observed to be the most released element in other MG compositions during aging in deionized water [49]. Cross-sectional observation of near-surface morphology by TEM-EDS revealed that Cu depletion resulted in a nanoporous network in a Pd-based MG, and a nanocrystalline embedded oxide layer in Ti-based MGs [49]. To sum up, the uniform element

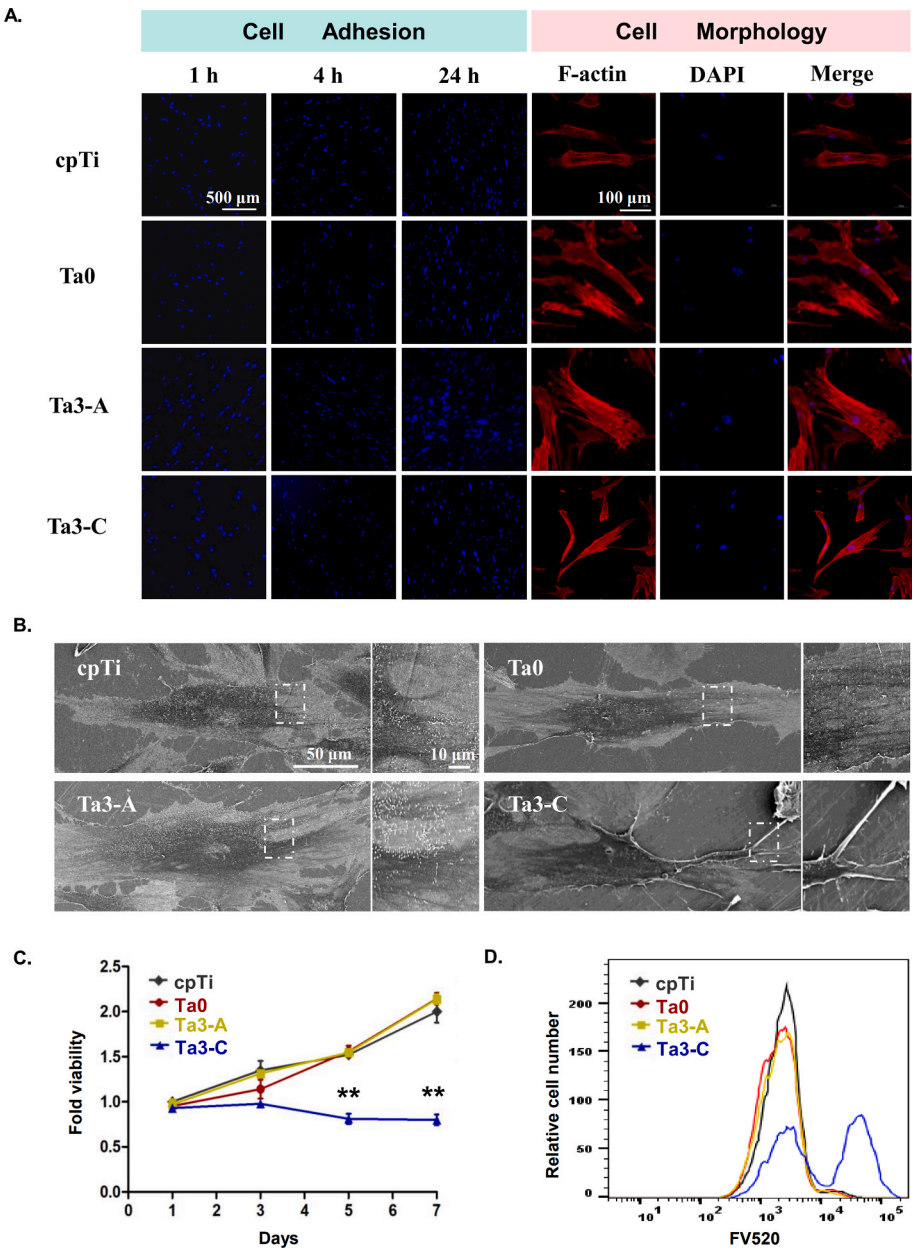

Fig. 3. Cell adhesion, morphology and viability features. A) (Left) Representative cell adhesion figures at 1 h, 4 h and 24 h. Ta0 and Ta3–C exhibited inferior initial cell adhesion of BMSCs at 1 h and 4 h. (Right) Phalloidin staining of BMSCs F-actin at 24 h. B) SEM images of BMSCs cell morphology on material surface at 24 h. C) Relative BMSCs cell viability fold change of all samples, indicating that Ta3–C significantly inhibited cell viability at day 5 and day 7. Data are presented as mean ± SE. $^{**}p < 0.01$. D) Flow cytometry result of FV520 staining of all samples, indicating a population shift from living to necrotic BMSCs that co-cultured with Ta3–C for 5 days.

distribution and excellent chemical stability of Ta3-A provided a more stable and biocompatible context for BMSCs. Atomic structural change to crystalline largely hampered cell adhesion, morphology and viability. Therefore Ta3–C was dropped for further analysis on biological effects as it didn't meet the fundamental biosafety demand of endosseous implants.

3.4. Macrophage responses

The foreign body response upon biomaterial implantation triggers an immunological host reaction that is largely influenced by the polarization state of macrophages [19]. Macrophages incubating 48 h with Ta0 and Ta3-A secreted significantly less pro-inflammatory IL-1β and TNF-α, and Ta3-A mildly elevated the production of anti-inflammatory IL-10 (Fig. 5A). 10-fold down-regulation of *Il-1b* and *iNos* gene expression marked a pronounced inhibition of M1-related inflammation, while the expression of M2-related genes *Il-10*, were only found significant between cpTi and Ta3-A (Fig. 5B). These results implied that compared to cpTi, Zr-MGs appeared to be a milder inflammatory stimulus to bone marrow macrophages. Less ruffling and activated M1 morphology of RAW264.7 was observed in another reported Zr-MGs, and the secretion of TNF-α was also reduced on three consecutive days of culturing, suggesting less inflammation evoked by the Zr-based MGs [50].

RNA-sequencing sorted out 113 and 234 differentially expressed genes between Ta3-A vs cpTi and Ta0 vs cpTi (Fig. S6A). Among the 88 overlapping genes, many inflammation-related genes were down-regulated in Ta0 and Ta3-A, with *iNos* (referred as *Nos2* in the heatmap) being the top 5 (Fig. 5C). While gene ontology and KEGG analysis

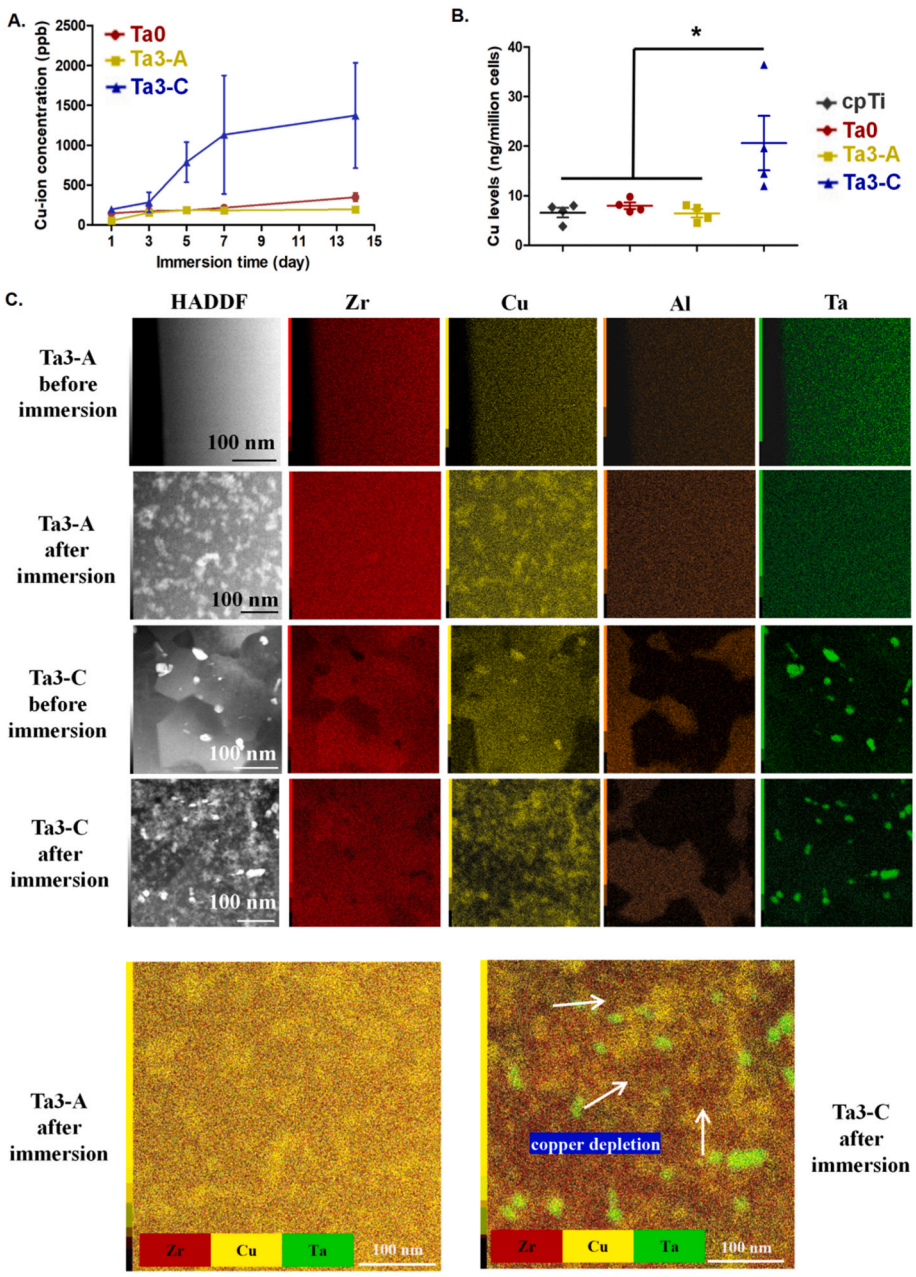

Fig. 4. Ion release features related to material surface chemistry and atomic structure. A) The release of Cu ions in α-MEM at 37 °C measured by ICP-MS. A dramatic increase of ion releases was observed after 5 days in Ta3–C. Data are presented as mean ± SD. B) The intracellular Cu ion levels detected by ICP-MS. After incubating with Ta3–C for 5 days, BMSCs absorbed significantly more Cu ions, compromising cell viability. Data are presented as mean ± SE. $*p < 0.05$. C) Chemical analysis of Ta3-A and Ta3–C before and after being immersed in α-MEM at 37 °C for 5 days. High angle angular dark field detector (HADDF) images showed Cu depletion at the near surface of Ta3–C.

(Figs. S6B and C) revealed that mutual differentially expressed genes were mostly enriched in immune response, we discovered that macrophage-derived osteoclast differentiation and NF-κB signaling were also down-regulated in Ta0 and Ta3-A, indicating a better bone forming osteoimmune environment.

Western blot verified that iNos was significantly decreased in Ta0 and Ta3-A, as well as the M1 phenotype marker Cd80 (Fig. 5D). Notably, there was a slight increase in M2 phenotype marker Cd206 in Zr-BMGs, especially in Ta3-A, indicating a functional shift from inflammatory to reparative macrophage phenotype. Cellular intake of tantalum nanoparticles induced less ROS and pro-inflammatory cytokines than TiO_2 nanoparticles in THP-1-derived macrophages [51]. Tantalum nanoparticles had also been demonstrated to promote M2 polarization by up-regulating *Il-10* and *Tgf-b1*, but not *Arg-1* [52]. This biological feature of Ta may partly explain the better reparative performance of Ta3-A over Ta0 in Il-10 gene expression and cytokine production. IL-10 was considered as a suppressor of inflammatory reactions and osteoclast differentiation [53]. For another, Hotchkiss et al. suggested that high-hydrophilic surfaces improved M2 activation observed as higher *Il-10* and *Tgf-b1* expression [54]. Coincidentally, we found that the contact angle was significantly lower in Ta3-A, in contrast to Ta0. Taken together, we proposed that it might be a common characteristic of Zr-MGs to evoke less inflammatory foreign body response, priming an osteoimmune context for osseointegration. The addition of Ta endowed Zr-MGs with an improved reparative response favoring M2 activation.

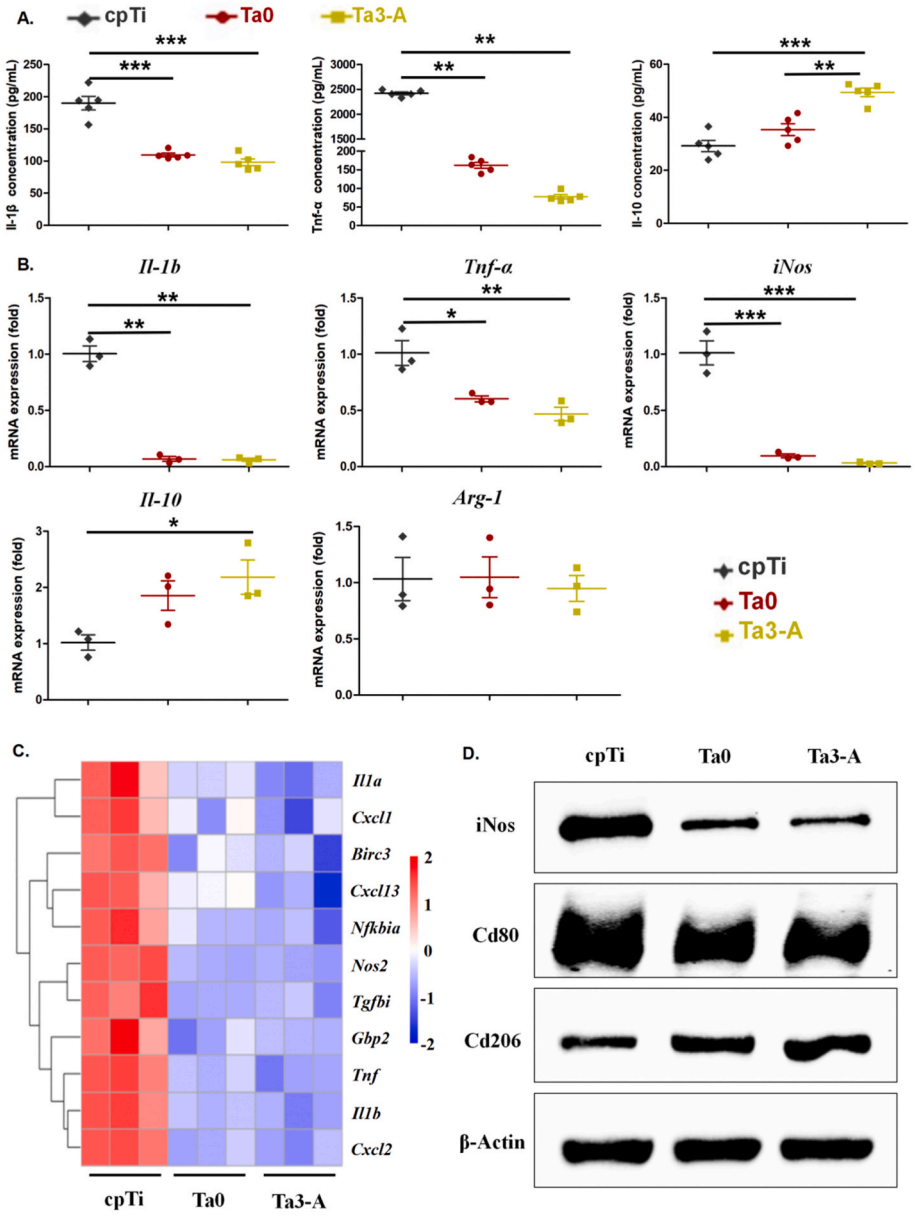

Fig. 5. Macrophage responses to different surface chemistry. A) ELISA results of IL-1β, TNF-α and IL-10. Ta0 and Ta3-A significantly suppressed the secretion of pro-inflammatory cytokines. B) qRT-PCR results of M1 and M2 activity related markers. Ta0 and Ta3-A significantly reduced the expression of pro-inflammatory markers. C) Heatmap of representative overlapped genes between Ta3-A vs cpTi and Ta0 vs cpTi comparisons, showing an overall decrease in pro-inflammatory genes. D) Western blot result of iNos, Cd80, Cd206 and β-actin. Data are presented as mean ± SE. $^{*}p < 0.05$, $^{**}p < 0.01$ and $^{***}p < 0.001$.

3.5. The angiogenesis reaction

Angiogenesis starts when the primitive granulation tissue needs to be replaced by BMSCs, along with their secreted fibers and matrix [55]. The ingrowth and vascularization of endothelial cells are key to support osseointegration. Human umbilical vein endothelial cells (HUVECs) exhibited better initial proliferation on Ta3-A at the first day of incubation (Fig. S7A), which was also reported in a Zr–Al–Fe–Cu MG compared to 316L SS [56]. HUVECs cultured in material extracts were subjected to scratch assays (Fig. 6A), and quantitative measurements proved that Ta0 and Ta3-A had more advantage over cpTi in inducing wound healing. In the meantime, the prominent effect of Ta3-A on tube formation was demonstrated as more interconnected vascular networks and larger cell tubules in contrast to cpTi and Ta0 throughout the observation time points at 4 h, 8 h and 12 h (Fig. 6A and Fig. S7C). qRT-PCR revealed that angiogenesis-related markers, *VEGF* and *CD31*, were significantly up-regulated in Ta3-A after 3 days of co-culturing (Fig. 6B).

To unravel the potential mechanism underlying the preferred angiogenesis reaction of HUVECs on Ta3-A, RNA-sequencing was performed. 1950 and 1677 differentially expressed genes were detected between Ta3-A vs cpTi and Ta3-A vs Ta0, *respectively* (Fig. S7D). The heatmap presented the relative higher expression of some important genes regulating angiogenesis in Ta3-A, compared with Ta0 and cpTi (Fig. S7D). Interestingly, we also noticed some osteogenesis-related markers, such as *BMP2*, *SMAD1* and *AKT1*, were significantly elevated in Ta3-A, indicating a potential cross-talk to promote bone formation. GSEA further revealed that Ta3-A exhibited positive regulation on angiogenesis and vasculature development (Fig. S7E), as well as promoting VEGF production (Fig. 6C). Immunofluorescent staining confirmed the increased protein expression of VEGF in Ta3-A, with a statistical significance against cpTi (Fig. 6D).

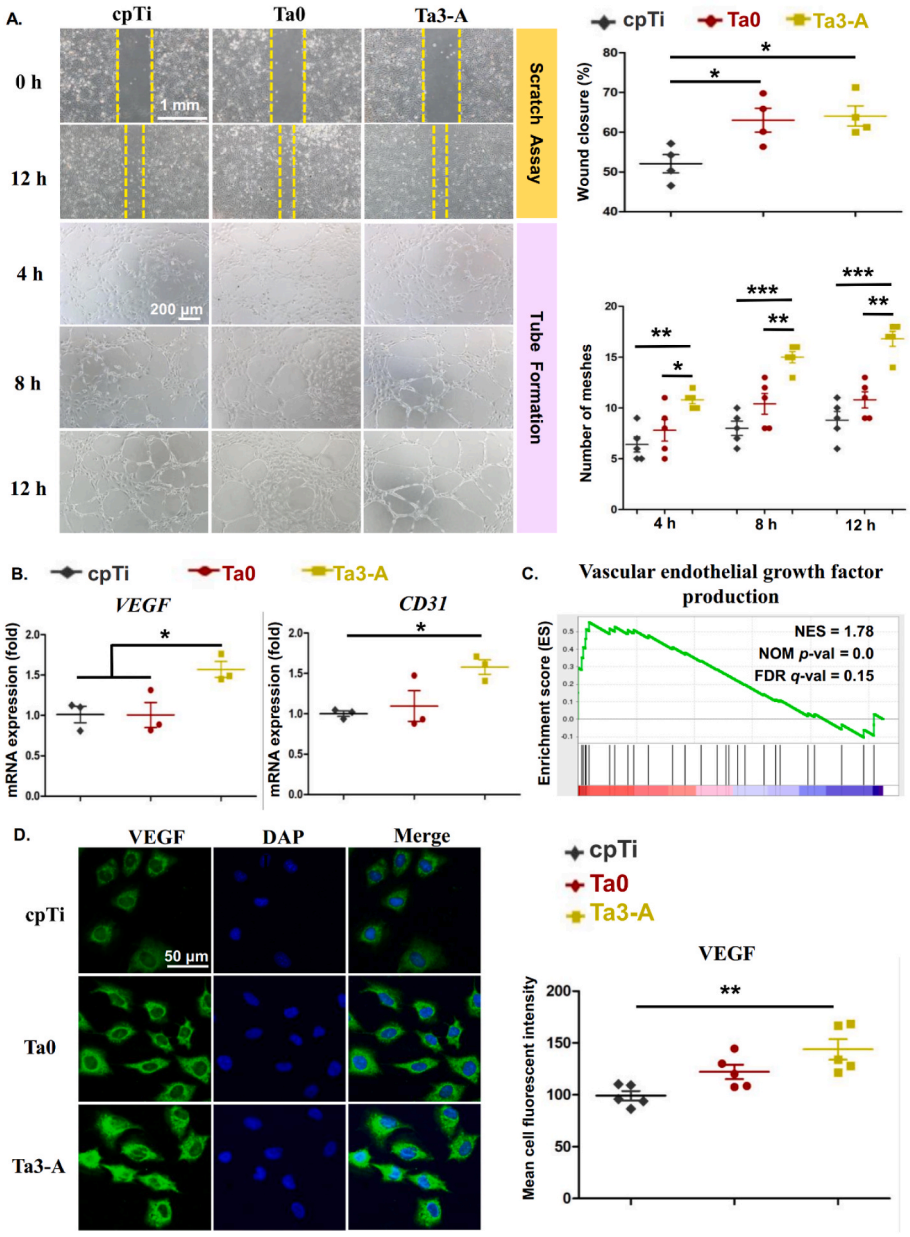

Fig. 6. The angiogenesis reaction to different surface chemistry. A) (Top) Scratch assay and quantitative measurement of HUVECs cultured in material's extract, indicating better wound healing in Ta0 and Ta3-A. (Bottom) Representative images and quantitative measurement of tube formation assay at 4 h, 8 h and 12 h, indicating that Ta3-A could efficiently promote vasculature development. B) qRT-PCR of angiogenesis marker, *VEGF* and *CD31*. C) GSEA of GO found expression enrichment of Ta3-A in VEFG production (GO: 0010573) when compared to that of cpTi. D) Immunofluorescent staining of VEGF, confirming that Ta3-A up-regulated the protein level of VEGF in comparison with cpTi. Data are presented as mean ± SE. $*p < 0.05$, $**p < 0.01$ and $***p < 0.001$.

Tantalum nanoparticles (TaNPs) coatings had direct effect on improving microvascular network formation and migration, while up-regulating the expression of pro-angiogenic marker *Vegf*, *Ang-1* and *eNos* of endothelial progenitor cells *in vitro* [57–59]. In the meantime, *in vivo* implantation of TaNPs-coated PCL enabled better neo-vascularization and coupled bone regeneration by elevating CD31 expression [58,59]. Tantalum nanotubes also shortly increased the *FGFR* expression in HUVECs [60]. Further, 5 μg/mL treatment TaNPs promoted IL-4 induced M2 macrophage's expression of *Vegf*, implying an indirect angiogenic effect [52]. Consistently, we observed that Ta3-A exhibited higher VEGF expression than cpTi at both mRNA and protein level. There is a lack of study solely focusing on the angiogenic effect of Ta in its metallic form [61], yet we observed that Ta could exhibit a positive regulation on angiogenesis in its amorphous state. Previous researches found that $Zr_{61}Cu_{25}Al_{12}Ti_2$ promoted HUVECs migration and tube formation, as well as the mRNA expression of *VEGF* and *vWF in vitro*, while improving vascular formation around implants *in vivo* [2,62]. The authors attributed the enhanced angiogenic ability of $Zr_{61}Cu_{25}Al_{12}Ti_2$ to the presence of Cu. Indeed, various reports pointed out the proangiogenic role of Cu through several pathways, with VEGF signaling pathway being the most prominent [61]. It is worth mentioning that GSEA failed to reach a statistical significance in VEGF

production between Ta0 and cpTi. We assumed that Ta enlarged the angiogenic effect of Zr-MGs. Interestingly, we observed the ion release level of Al in Ta0 almost tripled that of Ta3-A in ECM material extracts (Fig. S7B). This coincided with the result in the α-MEM (Fig. S4B). We assumed that the addition of Ta helped to stabilize Al in the alloy system. Proteomic analysis revealed a significantly elevated expression of an angiogenic inhibitor, thrombospondin-1 (THBS1), and its associated signaling pathway in mouse E10 alveolar epithelial cells treated with 100 μg/mL 10 nm-Al_2O_3-modified carbon nanotubes [63,64]. Similarly, we also detected a 1.8-fold significantly higher gene expression of *THBS1* in Ta0 compared to Ta3-A in our RNA-seq data (Fig. S7D), implying an adverse effect of Al might somehow counteract the angiogenic role of Cu. Future studies focusing on the regulation of Al on angiogenesis and its potential interaction with other ions may help to dissect this issue.

3.6. The osteogenic potential

The recruitment, differentiation, ossification and biomineral formation of mesenchymal cells at implant surface contribute to the basis of osseointegration. BMSCs were directly cultured on materials' surface to evaluate their osteogenic potential. Ta3-A greatly pronounced the ALP activity at 7 days and extracellular matrix mineralization at 14 days, as evidenced by intensified staining and statistically elevated quantification (Fig. 7A). Osteogenesis related genes, *SP7*, *ALPL* and *BGLAP*, were significantly up-regulated in Ta3-A after 7 days of osteoinduction (Fig. 7B). Enhanced *ALPL* and *COL1* expression were also observed in MG63 cells cultured on $Zr_{61}Cu_{25}Al_{12}Ti_2$ [46]. Besides, Pt-, Pd- and Ti-based MGs could induce better mineralization than titanium alloy as well [49].

RNA-sequencing further revealed the increased expression of many osteogenic promoting genes, such as *PTH1R*, *IGF1*, *BMP4*, *BMP7* and *ECM1/2*, in Ta3-A (Fig. 7C). Moreover, many differentially expressed genes were categorized as genes regulating skeletal system development, ossification, extracellular matrix organization and osteoblast differentiation by GO analysis, indicating a more regulatory role of Ta3-A in osteogenesis compared to cpTi and Ta0 (Figs. S8A–F). Gene sets comparison of Ta3-A against cpTi or Ta0 calculated high enrichment score in ossification and osteoblast differentiation as well (Fig. S8G). Terms as positive regulation of angiogenesis and positive regulation of vasculature development were found in Ta3-A (Figs. S8B and D), confirming its ability to mediate the cross-talk between osteogenesis and angiogenesis.

Noticeably, both GO analysis and GSEA on KEGG pathway pointed out transforming growth factor-beta (TGF-β) and bone morphogenic protein (BMP) signaling pathway as a potential molecular mechanism whereby Ta3-A might regulate osteogenesis (Fig. 7D and Figs. S8B and D). The up-regulation of TGF-β/BMP signaling pathway related genes sorted out by RNA-sequencing, *BMP4* and *SMAD9* (commonly known as SMAD8, now officially named as SMAD9 by NCBI), were confirmed by qRT-PCR (Fig. 7E). The well-studied canonical SMAD-dependent TGF-β/BMP signaling pathway is comprised of two signaling pathways: TGF-β signaling, mediated by TGF-β1-3 through SMAD2/3, and BMP signaling, mediated by BMP ligands through SMAD1/5/9 [65]. Based on the level of differentially expressed genes, we argued that BMP signaling was more likely to be in concerned. Western blot analysis demonstrated an obvious increase in BMP4 and total SMAD9 expression in Ta3-A (Fig. 7F). The elevated BMP4 then largely intensified the phosphorylation of SMAD1/5/9 complex in Ta3-A, activating osteoblast differentiation and maturation [65]. The up-regulated protein expression of ALPL was evidenced as a downstream functioning marker that contributed to the improved osteogenesis in Ta3-A, compared to cpTi and Ta0.

The osteoinductive effect was considered to be the most pronounced biological role of Ta in many well-established works. By direct surface contacting, Ta was discovered to modulate robust osteogenesis through BMP signaling pathway, in both normal and compromised bone forming context [6]. Micro-patterned Ta coatings could more efficiently elevate the expression of *SMAD1*, *RUNX2* and *ALPL* than Ti in hMSCs at 14 days [66]. Ta nanoparticles with size of 3–5 nm exhibited the most prominent ability to induce osteogenesis by increasing genes as *Runx2*, *Alpl* and *Bmp2*, in comparison to PEEK and Ta nanoparticles with size of 20 nm [9]. Knockdown of either Runx2 or Smad1 could significantly decrease the expression of Runx2 and Alpl, as well as the ALP activity, indicating that the osteogenic effect of pure Ta was mediated through Bmp2/Smad1 signaling pathway in ovariectomized rat BMSCs [39]. Notably, transcriptomic profiling revealed that *BMP4* was the most up-regulated genes in the mandibular bone of patients receiving porous tantalum implants after 2 weeks, which was about 6-fold higher than that of titanium alloy [67]. *ALPL*, *DLX5* and *RUNX2* were also increased as a consequence of enhanced BMP signaling pathway [67]. Similar results were observed in osteopenic patients by the same research group [68]. Taken the current studies into consideration, we concluded that the amorphous state of Ta3-A provided BMSCs a uniform contact with Ta, which in turn triggered the BMP signaling pathway to improve osteoblast differentiation and bone formation.

3.7. Osseointegration

The direct bone-implant contact without fibrous tissue is the essence of osseointegration. Ta3-A implants showed an advantageous ability to induce new bone formation compared to that of cpTi at 4 weeks post implantation surgery (Fig. 8A and B). This advantage proceeded to 8 weeks as significantly more bone volume with increasing number of trabeculae and less separation were quantified by Micro-CT analysis (Fig. 8A, B and Fig. S10A). No significant difference was observed between Ta3-A and Ta0 by Micro-CT analysis. However, histological analysis of hard tissue sections revealed less direct bone-implant contact area and length around Ta0 implants than Ta3-A at 8-week post-surgery (Fig. 8C and D). This inconsistency was due to the influence of metal artifacts that could not be fully eliminated, emphasizing the importance of direct histological observation. Although having less bone area, the quality of osseointegration defined by the direct bone-implant-contact percentage of cpTi was comparable to that of Ta3-A (Fig. 8C and D), indicating that Ta3-A was more efficient in promoting bone formation, thus the quantity of osseointegration. This assumption was further supported by the dynamic measurement of double-fluorescent labeling where the distance between the ARS and calcein represented the new bone formed between 4 and 8 weeks post implantation (Fig. 8F). Ta3-A exhibited the fastest mineral apposition rate (MAR) during this time (Fig. 8E), suggesting that Ta3-A improved osseointegration by accelerating new bone formation around biomedical implants.

Zr-BMGs $Zr_{70}Ni_{16}Cu_6Al_8$ and $Zr_{61}Cu_{25}Al_{12}Ti_2$ were demonstrated to facilitate *in vivo* osseointegration. $Zr_{70}Ni_{16}Cu_6Al_8$ exhibited increased implant stability, bone-to-implant contact and bone area upon oblique loading for 7 and 28 days, in contrast with grade 2 pure titanium, suggesting a better response to mechanical stimuli on osseointegration [25]. $Zr_{61}Cu_{25}Al_{12}Ti_2$ was able to induce more vascular networks around implants, improving better osteogenesis and chondrogenesis and relieving the pain level during recovery [2]. Despite the presence of complex metal elements in MGs, researchers didn't find significant difference in metal ion levels in blood or important organs that could cause pathological changes in livers and kidneys [69]. Similarly, only a transient elevation of blood ALP level was detected in rats implanted with Ta3-A at 4 weeks, which might possibly be related with the active osteogenesis at that time. No inflammations or pathological features were observed in cpTi and our two Zr-MGs (Figs. S10B–D).

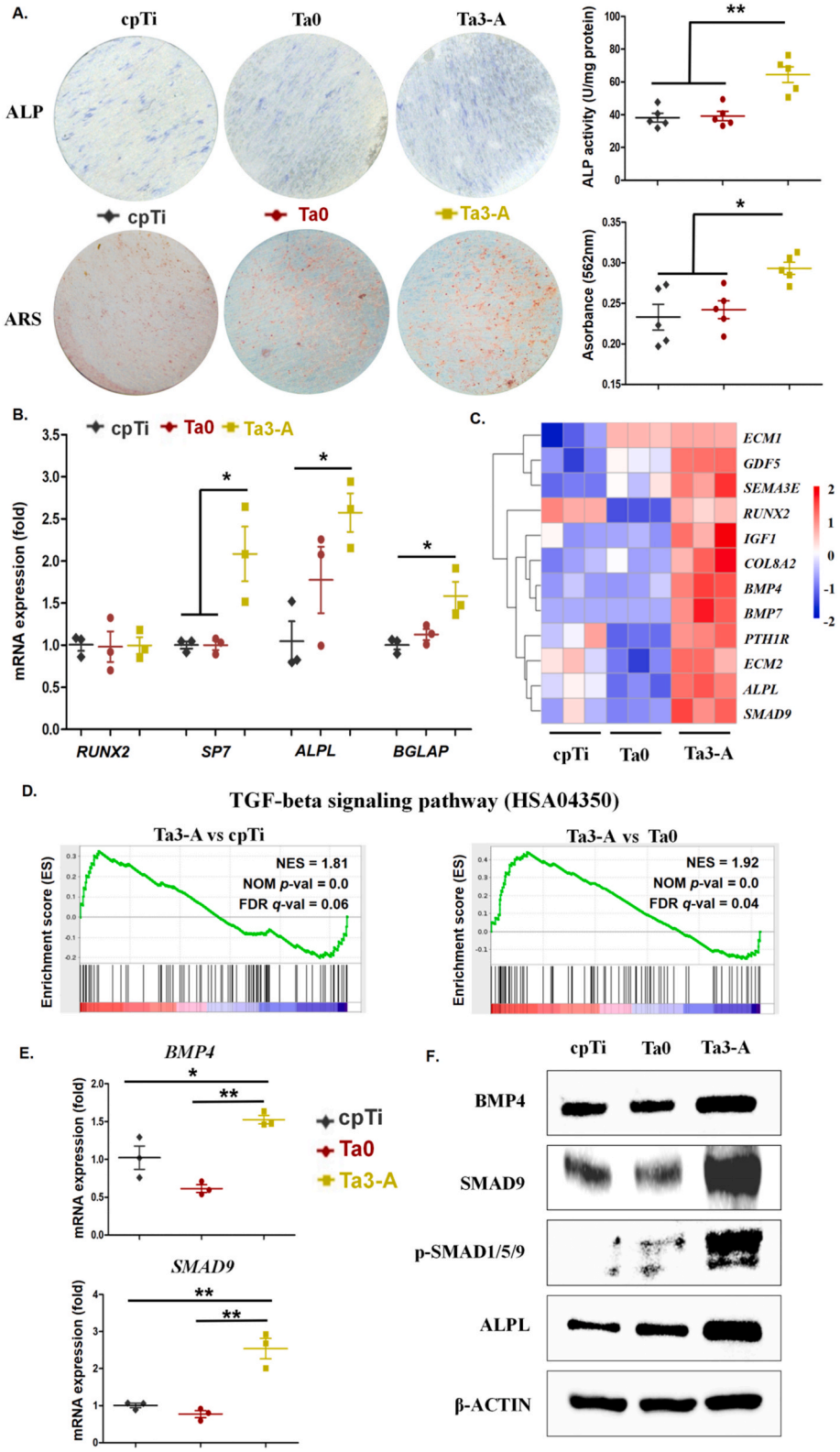

Fig. 7. The osteogenic potential of different surface chemistry. A) (Top) ALP staining on cpTi, Ta0 and Ta3-A surface, and quantitative measurement of ALP activity. Ta3-A showed enhanced ALP activity. (Bottom) ARS staining on cpTi, Ta0 and Ta3-A surface, and dissolved ARS OD value measured at A562 nm. Ta3-A showed exhibited better calcium nodules formation. B) qRT-PCR of osteogenic markers. Ta3-A significantly increased the expression of *SP7*, *ALPL* and *BGLAP*. C) Heatmap showing the expression of representative osteogenic genes in investigated materials. D) GSEA of KEGG found expression enrichment of Ta3-A in regulating TGF-beta signaling pathway (HSA04350) in comparison with cpTi and Ta0. Note that in KEGG pathway, TGF-beta signaling pathway encompassed "TGF-β signaling pathway" and "BMP signaling pathway" (https://www.kegg.jp/pathway/map=map04350&keyword=TGF-Beta). E) qRT-PCR results confirmed the elevated expression of BMP4 and SMAD9 in Ta3-A. F) Western blot of BMP4, total SMAD9, phosphorylated SMAD1/5/9, ALPL and β-actin. Results indicated an up-regulated and activated BMP signaling pathway in Ta3-A. Data are presented as mean ± SE. $*p < 0.05$ and $**p < 0.01$.

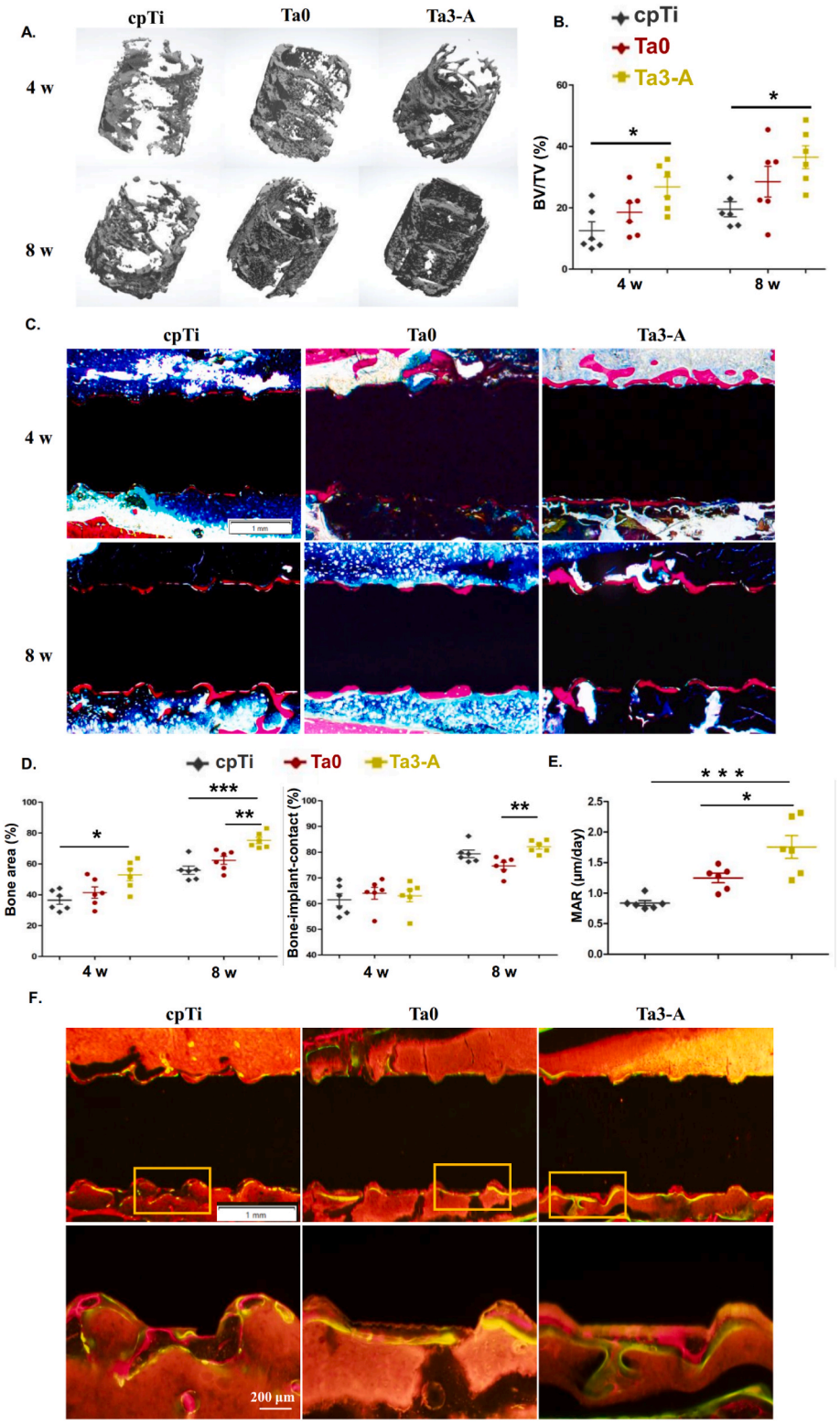

Fig. 8. Osseointegration on different surface chemistry. A) 3D reconstruction of peri-implant bone at 4- and 8-weeks post-implantation. B) Micro-CT analysis of bone volume to total volume fraction, indicating an inferior quantity of peri-implant bone around cpTi implants than that of Ta3-A. C) Representative images of Stevenel's blue and Van Gieson's picrofuchsin staining showing new bone formation around implants. Ta3-A implants were able to induce more bone formation that was in direct close contact to implant surfaces. D) Quantitative measurement of bone area percentage around implants and relative bone-implant-contact length. Ta3-A implants achieved better osseointegration than Ta0. E) Quantitative analysis of dynamic mineral apposition rate (MAR) between 4 and 8 weeks. Ta3-A implants induced faster bone formation rate. F) Immunofluorescent images merged from ARS at 4 weeks and calcein green at 8 weeks. The distance between the two immunofluorescent lines represented the new bone formed during 4–8 weeks. Data are presented as mean ± SE. *$p < 0.05$, **$p < 0.01$ and ***$p < 0.001$.

4. Conclusions

For one, this study provided a glance at how the single element addition, achieved by the substitution of Zr with Ta, affected the properties and biological processes in a Zr–Cu–Al MG composition. From the surface chemistry aspect, it could be concluded as follows:

- When compared to cpTi, Ta3-A significantly reduced the inflammatory response of M1 macrophage while improving the reparative M2 macrophage activity; increased angiogenesis through VEGF signaling pathway; pronounced *in vitro* osteogenesis via BMP signaling pathway and *in vivo* bone formation. Only a few of these cellular effects were significantly observed in Ta0 in contrast to cpTi, suggesting that Ta intensified and broadened the regulatory role of Zr–Cu–Al MGs as endosseous implants.
- When compared to Ta0, the addition of Ta increased the surface hydrophilicity, compressive strength and corrosion resistance; increased the chemical stability by forming a more stable oxide passive film; slightly improved the secretion of anti-inflammatory cytokine Il-10, moderately enhanced the angiogenesis effect, largely promoted the osteogenic potential through BMP signaling pathway, and thus finally achieving a better osseointegration. These improved biological effects were mostly in line with reported features of tantalum metal, coatings and nanoparticles that provided a uniform and direct material-cell contact. In overall, the amorphous state of Ta not only retained the favorable biological functions of Ta, but also increased some aspects of mechanical, physical and chemical properties of Zr–Cu–Al MGs, achieving an advanced functional material as $Zr_{58}Cu_{25}Al_{14}Ta_3$.

For another, the comparison between the Ta3-A and Ta3–C drew attentions to the influence of atomic structure on chemical stability in physiologically relevant environment and cell viability. The lack of crystal phases and uniform element distribution in Ta3-A guaranteed less ion releases below the safety limit, thus ensuring cell viability.

Further studies can make deeper explorations into the above two aspects by systematic screening using high-throughput methods to optimize the composition and obtain a Zr–Cu–Al–Ta MG composition with the most balanced characteristics, as well as modifying the annealing conditions to obtain different crystalline microstructures to find the acceptable safety degree of crystallization so as to set a standard for future industrial fabrication as potential endosseous implants.

Data availability

All RNA-Seq data have been deposited into NCBI database with the identifier GSE252671.

CRediT authorship contribution statement

Yunshu Wu: Writing – review & editing, Writing – original draft, Validation, Methodology, Investigation, Funding acquisition, Formal analysis, Data curation, Conceptualization. **Feifei Wang:** Validation, Investigation, Formal analysis, Data curation. **Yao Huang:** Validation, Methodology, Investigation, Data curation. **Fu Zheng:** Investigation, Data curation. **Yuhao Zeng:** Methodology, Data curation. **Zhen Lu:** Supervision. **Songlin Wang:** Supervision, Resources. **Baoan Sun:** Writing – review & editing, Supervision, Resources, Project administration, Methodology, Funding acquisition, Conceptualization. **Yuchun Sun:** Writing – review & editing, Supervision, Resources, Funding acquisition, Conceptualization.

Declaration of competing interest

The authors declare no conflict of interest.

Acknowledgements

The research was financially supported by the National Natural Science Foundation of China (52035001), National Key R&D Program of China (2019YFB1706904), Beijing Training Project for the Leading Talents in S & T (Z191100006119022), National Key Research and Development Plan (2018YFA0703603), National Science 535 Foundation of China (52192602), and Youth Fund of the National Natural Science Foundation of China (82201125).

Appendix A. Supplementary data

Supplementary data to this article can be found online at https://doi.org/10.1016/j.bioactmat.2024.04.014.

References

[1] H.F. Li, Y.F. Zheng, Recent advances in bulk metallic glasses for biomedical applications, Acta Biomater. 36 (2016) 1–20. https://10.1016/j.actbio.2016.03.047.
[2] K. Sun, R. Fu, X.W. Liu, L.M. Xu, G. Wang, S.Y. Chen, Q.J. Zhai, S. Pauly, Osteogenesis and angiogenesis of a bulk metallic glass for biomedical implants, Bioact. Mater. 8 (2022) 253–266. https://10.1016/j.bioactmat.2021.06.018.
[3] X. Liu, C. Ding, P.K. Chu, Surface modification of titanium, titanium alloys, and related materials for biomedical applications, Mater. Sci. Eng. R 47 (2004) 49–121. https://10.1016/j.mser.2004.11.001.
[4] S. Gautam, D. Bhatnagar, D. Bansal, H. Batra, N. Goyal, Recent advancements in nanomaterials for biomedical implants, Biomed. Eng. Adv. 3 (2022). https://10.1016/j.bea.2022.100029.
[5] S. Nagarajan, M. Mohana, P. Sudhagar, V. Raman, T. Nishimura, S. Kim, Y.S. Kang, N. Rajendran, Nanocomposite coatings on biomedical grade stainless steel for improved corrosion resistance and biocompatibility, ACS Appl. Mater. Interfaces 4 (2012) 5134–5141. https://10.1021/am301559r.
[6] H. Qian, T. Lei, Z. Ye, Y. Hu, P. Lei, From the performance to the essence: the biological mechanisms of how tantalum contributes to osteogenesis, BioMed Res. Int. 2020 (2020) 1–8. https://10.1155/2020/5162524.
[7] X. Wang, B. Ning, X. Pei, Tantalum and its derivatives in orthopedic and dental implants: osteogenesis and antibacterial properties, Colloids Surf. B Biointerfaces 208 (2021) 112055. https://10.1016/j.colsurfb.2021.112055.
[8] D.P. Gopinath Mani, K. Grove, S. Collins, A. Ornberg, R. Shulfer, A comprehensive review of biological and materials properties of Tantalum and its alloys, J. Biomed. Mater. Res. 110 (2022) 1291–1306. https://10.1002/jbm.a.37373.
[9] T. Lu, J. Wen, S. Qian, H. Cao, C. Ning, X. Pan, X. Jiang, X. Liu, P.K. Chu, Enhanced osteointegration on tantalum-implanted polyetheretherketone surface with bone-like elastic modulus, Biomaterials 51 (2015) 173–183. https://10.1016/j.biomaterials.2015.02.018.
[10] R. Wauthle, J. van der Stok, S. Amin Yavari, J. Van Humbeeck, J.P. Kruth, A. A. Zadpoor, H. Weinans, M. Mulier, J. Schrooten, Additively manufactured porous tantalum implants, Acta Biomater. 14 (2015) 217–225. https://10.1016/j.actbio.2014.12.003.
[11] C. Suryanarayana, A. Inoue, Bulk Metallic Glasses, second ed., CRC Press, Florida, 2018.
[12] J. Li, J.A. Jansen, X.F. Walboomers, J.J. van den Beucken, Mechanical aspects of dental implants and osseointegration: a narrative review, J. Mech. Behav. Biomed. Mater. 103 (2020) 103574. https://10.1016/j.jmbbm.2019.103574.
[13] R.T. Ott, C. Fan, J. Li, T.C. Hufnagel, Structure and properties of Zr–Ta–Cu–Ni–Al bulk metallic glasses and metallic glass matrix composites, J. Non-Cryst. Solids 317 (2003) 158–163. https://10.1016/s0022-3093(02)01996-8.
[14] X.H.H. Kou, X. Liu, X. Song, G. Chen, K. Yao, Effects of small amount Ta on the characteristics of the Zr-Al-Ni-Cu-Ta bulk metallic glass, J. Univ. Sci. Technol. Beijing 12 (2005) 257.
[15] K.A. Pacheco, Allergy to surgical implants, Clin. Rev. Allergy Immunol. 56 (2018) 72–85. https://10.1007/s12016-018-8707-y.
[16] J.P. Chu, T.-Y. Liu, C.-L. Li, C.-H. Wang, J.S.C. Jang, M.-J. Chen, S.-H. Chang, W.-C. Huang, Fabrication and characterizations of thin film metallic glasses: antibacterial property and durability study for medical application, Thin Solid Films 561 (2014) 102–107. https://10.1016/j.tsf.2013.08.111.
[17] J.P. Chu, C.-C. Yu, Y. Tanatsugu, M. Yasuzawa, Y.-L. Shen, Non-stick syringe needles: beneficial effects of thin film metallic glass coating, Sci. Rep. 6 (2016) 31847. https://10.1038/srep31847.
[18] C.-H. Chang, C.-L. Li, C.-C. Yu, Y.-L. Chen, S. Chyntara, J.P. Chu, M.-J. Chen, S.-H. Chang, Beneficial effects of thin film metallic glass coating in reducing adhesion of platelet and cancer cells: clinical testing, Surf. Coating. Technol. 344 (2018) 312–321. https://10.1016/j.surfcoat.2018.03.040.
[19] R. Trindade, T. Albrektsson, P. Tengvall, A. Wennerberg, Foreign body reaction to biomaterials: on mechanisms for buildup and breakdown of osseointegration, Clin. Implant Dent. Relat. Res. 18 (2016) 192–203. https://10.1111/cid.12274.
[20] J.M. Brown, R.G. Mcqueen, Phase transitions, Grüneisen parameter, and elasticity for shocked iron between 77 GPa and 400 GPa, J. Geophys. Res. Solid Earth 91 (1986) B7. https://10.1029/JB091iB07p07485.
[21] Krautkramer & Josef, Ultrasonic Testing of Materials, third ed., Springer-Verlag, Berlin, 1983.

[22] L. Huang, Y. Yokoyama, W. Wu, P.K. Liaw, S. Pang, A. Inoue, T. Zhang, W. He, Ni-free Zr-Cu-Al-Nb-Pd bulk metallic glasses with different Zr/Cu ratios for biomedical applications, J. Biomed. Mater. Res. Part B, Appl. Biomater. 100 (2012) 1472–1482. https://10.1002/jbm.b.32715.

[23] C.D. Wagner, W.M. Riggs, L.E. Davis, J.F. Moulder, G.E. Muilenberg (Editor). Handbook of x-ray photoelectron spectroscopy: A reference book of standard data for use in x-ray photoelectron spectroscopy, first ed., Perkin-Elmer Corporation, Physical Electronics Division, Minnesota, 1979.

[24] P. Meagher, E.D. O'Cearbhaill, J.H. Byrne, D.J. Browne, Bulk metallic glasses for implantable medical devices and surgical tools, Adv. Mater. 28 (2016) 5755–5762. https://10.1002/adma.201505347.

[25] H. Ida, M. Seiryu, N. Takeshita, M. Iwasaki, Y. Yokoyama, Y. Tsutsumi, E. Ikeda, S. Sasaki, S. Miyashita, S. Sasaki, T. Fukunaga, T. Deguchi, T. Takano-Yamamoto, Biosafety, stability, and osteogenic activity of novel implants made of Zr(70)Ni(16)Cu(6)Al(8) bulk metallic glass for biomedical application, Acta Biomater. 74 (2018) 505–517. https://10.1016/j.actbio.2018.05.020.

[26] Y. Liu, Y.M. Wang, H.F. Pang, Q. Zhao, L. Liu, A Ni-free ZrCuFeAlAg bulk metallic glass with potential for biomedical applications, Acta Biomater. 9 (2013) 7043–7053. https://10.1016/j.actbio.2013.02.019.

[27] C. Bernard, V. Keryvin, Crystalline defects in bulk metallic glasses: consequences on fracture toughness determination and ductility, J. Phys. Condens. Matter. 32 (2020) 1–54, https://doi.org/10.1088/1361-648X/abaa7f.

[28] Q. Chen, G.A. Thouas, Metallic implant biomaterials, Mater. Sci. Eng. R Rep. 87 (2015) 1–57. https://10.1016/j.mser.2014.10.001.

[29] R.C.Y. Tam, C.H. Shek, Relaxation and crystallization of Zr41.2Ti13.8Cu12.5Ni10Be22.5 bulk amorphous alloys, Mater. Sci. Eng. 364 (2004) 198–201. https://10.1016/j.msea.2003.08.007.

[30] J. Fornell, E. Rossinyol, S. Suriñach, M.D. Baró, W.H. Li, J. Sort, Enhanced mechanical properties in a Zr-based metallic glass caused by deformation-induced nanocrystallization, Scripta Mater. 62 (2010) 13–16. https://10.1016/j.scriptamat.2009.09.014.

[31] J. Fornell, N. Van Steenberge, A. Varea, E. Rossinyol, E. Pellicer, S. Surinach, M. D. Baro, J. Sort, Enhanced mechanical properties and in vitro corrosion behavior of amorphous and devitrified Ti40Zr10Cu38Pd12 metallic glass, J. Mech. Behav. Biomed. Mater. 4 (2011) 1709–1717. https://10.1016/j.jmbbm.2011.05.028.

[32] F.K.J. Musil, H. Zeman, H. Polakova, Relationships between hardness, Young's modulus and elastic recovery in hard nanocomposite coatings, Surf. Coat. Technol. 154 (2002) 304–313. https://10.1016/S0257-8972(01)01714-5.

[33] W.H. Wang, L.L. Li, M.X. Pan, R.J. Wang, Supersoftening of transverse phonons in Zr41Ti14Cu12.5Ni10Be22.5 bulk metallic glass, Phys. Rev. B 62 (2000) 25–28. https://10.1103/PhysRevB.63.052204.

[34] E.M. Sherif, Y.A. Bahri, H.F. Alharbi, M.F. Ijaz, I.A. Alnaser, Influence of tantalum addition on the corrosion passivation of titanium-zirconium alloy in simulated body fluid, Materials 15 (2022). https://10.3390/ma15248812.

[35] W.H. Peter, R.A. Buchanan, C.T. Liu, P.K. Liaw, M.L. Morrison, J.A. Horton, C. A. Carmichael Jr., J.L. Wright, Localized corrosion behavior of a zirconium-based bulk metallic glass relative to its crystalline state, Intermetallics 10 (2002) 1157–1162. https://10.1016/S0966-9795(02)00130-9.

[36] V. Schroeder, C.J. Gilbert, R.O. Ritchie, Comparison of the corrosion behavior of a bulk amorphous metal, $Zr_{41.2}Ti1_{3.8}Cu_{12.5}Ni_{10}Be_{22.5}$, with its crystallized formScrip, Materials 38 (1998) 1481–1485. https://10.1016/S1359-6462(98)00089-X.

[37] S. Minagar, C.C. Berndt, C. Wen, Fabrication and characterization of nanoporous niobia, and nanotubular tantala, titania and zirconia via anodization, J. Funct. Biomater. 6 (2015) 153–170. https://10.3390/jfb6020153.

[38] L.A. Buchanan, A. El-Ghannam, Effect of bioactive glass crystallization on the conformation and bioactivity of adsorbed proteins, J. Biomed. Mater. Res. A 93 (2010) 537–546. https://10.1002/jbm.a.32561.

[39] P.-S. W, M.-M. Liu, X.-J. Guo, L.-L. Yin, H.-L. Cao, D. Zou, Osteoinductive effects of tantalum and titanium on bone mesenchymal stromal cells and bone formation in ovariectomized rats, Eur. Rev. Med. Pharmacol. Sci. 22 (2018) 7087–7104. https://10.26355/eurrev_201811_16241.

[40] M. Cihova, E. Müller, Y. Chandorkar, K. Thorwarth, G. Fortunato, K. Maniura-Weber, J.F. Löffler, M. Rottmar, Palladium-based metallic glass with high thrombogenic resistance for blood-contacting medical devices, Adv. Funct. Mater. 32 (2021) 2108256. https://10.1002/adfm.202108256.

[41] V.M. Villapun, F. Esat, S. Bull, L.G. Dover, S. Gonzalez, Tuning the mechanical and antimicrobial performance of a Cu-based metallic glass composite through cooling rate control and annealing, Materials 10 (2017) 506. https://10.3390/ma10050506.

[42] G.K. Jan Schroers, Thomas M. Hodges, Stephen Chan, Themis R. Kyriakides, Bulk Metallic Glasses for Biomedical Applications, J.O.M, 2009.

[43] N.J. Hallab, C. Vermes, C. Messina, K.A. Roebuck, T.T. Glant, J.J. Jacobs, Concentration- and composition-dependent effects of metal ions on human MG-63 osteoblasts, J. Biomed. Mater. Res. 60 (2010) 420–433. https://10.1002/jbm.10106.

[44] R. A. Yamamoto, M. Honma, Sumita, Cytotoxicity evaluation of 43 metal salts using murine fibroblasts and osteoblastic cells, J. Biomed. Mater. Res. A 39 (2015) 331–340, 10.1002/(SICI)1097-4636(199802)39:23.0.CO;2-E.

[45] L. Huang, Z. Cao, H.M. Meyer, P.K. Liaw, E. Garlea, J.R. Dunlap, T. Zhang, W. He, Responses of bone-forming cells on pre-immersed Zr-based bulk metallic glasses: effects of composition and roughness, Acta Biomater. 7 (2011) 395–405. https://10.1016/j.actbio.2010.08.002.

[46] J. Li, L.L. Shi, Z.D. Zhu, Q. He, H.J. Ai, J. Xu, Zr61Ti2Cu25Al12 metallic glass for potential use in dental implants: biocompatibility assessment by in vitro cellular responses, Mater. Sci. Eng., C 33 (2013) 2113–2121. https://10.1016/j.msec.2013.01.033.

[47] P. Tsvetkov, S. Coy, B. Petrova, M. Dreishpoon, A. Verma, M. Abdusamad, J. Rossen, L. Joesch-Cohen, R. Humeidi, R.D. Spangler, J.K. Eaton, E. Frenkel, M. Kocak, S.M. Corsello, S. Lutsenko, N. Kanarek, S. Santagata, T.R. Golub, Copper induces cell death by targeting lipoylated TCA cycle proteins, Science 375 (2022) 1254–1261. https://10.1126/science.abf0529.

[48] B.E. Kim, T. Nevitt, D.J. Thiele, Mechanisms for copper acquisition, distribution and regulation, Nat. Chem. Biol. 4 (2008) 176–185. https://10.1038/nchembio.72.

[49] W.A. Lackington, R. Wiestner, E. Pradervand, P. Schweizer, F. Zuber, Q. Ren, M. Stoica, J.F. Löffler, M. Rottmar, Surface chemistry dictates the osteogenic and antimicrobial properties of palladium-, platinum-, and titanium-based bulk metallic glasses, Adv. Funct. Mater. 33 (2023) 2302069. https://10.1002/adfm.202302069.

[50] L. Huang, T. Zhang, P.K. Liaw, W. He, Macrophage responses to a Zr-based bulk metallic glass, J. Biomed. Mater. Res. A 102 (2014) 3369–3378. https://10.1002/jbm.a.35009.

[51] L. Zhang, E.M. Haddouti, H. Beckert, R. Biehl, S. Pariyar, J.M. Ruwald, X. Li, M. Jaenisch, C. Burger, D.C. Wirtz, K. Kabir, F.A. Schildberg, Investigation of cytotoxicity, oxidative stress, and inflammatory responses of tantalum nanoparticles in THP-1-derived macrophages, Mediat. Inflamm. 2020 (2020) 1–14. https://10.1155/2020/3824593.

[52] Y. Sun, T. Liu, H. Hu, Z. Xiong, K. Zhang, X. He, W. Liu, P. Lei, Y. Hu, Differential effect of tantalum nanoparticles versus tantalum micron particles on immune regulation, Mater. Today Bio. 16 (2022) 100340. https://10.1016/j.mtbio.2022.100340.

[53] M. Baseri, F. Radmand, R. Hamedi, M. Yousefi, H.S. Kafil, Immunological aspects of dental implant rejection, BioMed Res. Int. 2020 (2020) 7279509. https://10.1155/2020/7279509.

[54] K.M. Hotchkiss, N.B. Ayad, S.L. Hyzy, B.D. Boyan, R. Olivares-Navarrete, Dental implant surface chemistry and energy alter macrophage activation in vitro, Clin. Oral Implants Res. 28 (2017) 414–423. https://10.1111/clr.12814.

[55] D.D. B. Giovanni E. Salvi, Niklaus P. Lang, Ingemar Abrahamsson, Tord Berglundh, Jan Lindhe, Saso Ivanovski, Nikos Donos, Temporal sequence of hard and soft tissue healing around titanium dental implants, Periodontol. 2000 68 (2015) 135–152. https://10.1111/prd.12054.

[56] L. Huang, C. Pu, R.K. Fisher, D.J.H. Mountain, Y. Gao, P.K. Liaw, W. Zhang, W. He, A Zr-based bulk metallic glass for future stent applications: materials properties, finite element modeling, and in vitro human vascular cell response, Acta Biomater. 25 (2015) 356–368. https://10.1016/j.actbio.2015.07.012.

[57] J. Nan, W. Liu, K. Zhang, Y. Sun, Y. Hu, P. Lei, Tantalum and magnesium nanoparticles enhance the biomimetic properties and osteo-angiogenic effects of PCL membranes, Front. Bioeng. Biotechnol. 10 (2022) 1038250. https://10.3389/fbioe.2022.1038250.

[58] K. Zhang, H. Hu, Y. Sun, J. Nan, W. Liu, P. Lei, Y. Hu, The bio-functionalized membrane loaded with Ta/WH nanoparticles promote bone regeneration through neurovascular coupling, Colloids Surf. B Biointerfaces 230 (2023) 113506. https://10.1016/j.colsurfb.2023.113506.

[59] W. Liu, K. Zhang, J. Nan, P. Lei, Y. Sun, Y. Hu, Nano artificial periosteum PCL/Ta/ZnO accelerates repair of periosteum via antibacterial, promoting vascularization and osteogenesis, Biomater. Adv. 154 (2023) 213624. https://10.1016/j.bioadv.2023.213624.

[60] S. Wu, X. Shen, M. Chen, K.H.R. Yie, Z. Zhou, M.A. Al-Baadani, K. Fang, A.M. Al-Bishari, Z. Deng, J. Liu, L. Yao, Multifunctional TaCu-nanotubes coated titanium for enhanced bacteriostatic, angiogenic and osteogenic properties, Mater. Sci. Eng., C 120 (2021) 111777. https://10.1016/j.msec.2020.111777.

[61] J. Durig, M. Calcagni, J. Buschmann, Transition metals in angiogenesis - a narrative review, Mater. Today Bio. 22 (2023) 100757. https://10.1016/j.mtbio.2023.100757.

[62] J. Li, H.J. Ai, The responses of endothelial cells to $Zr_{61}Ti_2Cu_{25}Al_{12}$ metallic glass in vitro and in vivo, Mater. Sci. Eng. C Mater. Biol. Appl. 40 (2014) 189–196. https://10.1016/j.msec.2014.03.051.

[63] G.M. Hilton, A.J. Taylor, S. Hussain, E.C. Dandley, E.H. Griffith, S. Garantziotis, G. N. Parsons, J.C. Bonner, M.S. Bereman, Mapping differential cellular protein response of mouse alveolar epithelial cells to multi-walled carbon nanotubes as a function of atomic layer deposition coating, Nanotoxicology 11 (2017) 313–326. https://10.1080/17435390.2017.1299888.

[64] J. Lawler, Thrombospondin-1 as an endogenous inhibitor of angiogenesis and tumor growth, J. Cell Mol. Med. 6 (2007) 1–12. https://10.1111/j.1582-4934.2002.tb00307.x.

[65] M. Wu, G. Chen, Y.P. Li, TGF-beta and BMP signaling in osteoblast, skeletal development, and bone formation, homeostasis and disease, Bone Res. 4 (2016) 16009. https://10.1038/boneres.2016.9.

[66] E. Kaivosoja, S. Myllymaa, Y. Takakubo, H. Korhonen, K. Myllymaa, Y. T. Konttinen, R. Lappalainen, M. Takagi, Osteogenesis of human mesenchymal stem cells on micro-patterned surfaces, J. Biomater. Appl. 27 (2013) 862–871. https://10.1177/0885328211428094.

[67] S. Bencharit, T. Morelli, S. Barros, J.T. Seagroves, S. Kim, N. Yu, K. Byrd, C. Brenes, S. Offenbacher, Comparing initial wound healing and osteogenesis of porous tantalum trabecular metal and titanium alloy materials, J. Oral Implantol. 45 (2019) 173–180. https://10.1563/aaid-joi-D-17-00258.

[68] E.K. Hefni, S. Bencharit, S.J. Kim, K.M. Byrd, T. Moreli, F.H. Nociti, S. Offenbacher, S.P. Barros, Transcriptomic profiling of tantalum metal implant osseointegration in osteopenic patients, BDJ Open 4 (2018) 17042. https://10.1038/s41405-018-0004-6.

[69] K. Imai, S. Hiromoto, In vivo evaluation of bulk metallic glasses for osteosynthesis devices, Materials 9 (2016) 676. https://10.3390/ma9080676.